MID-AMERICA TRANSPORTATION CENTER

Report # MATC-MS&T: 132-4

Final Report

WBS: 25-1121-0005-132-4

SMART Shear Keys for Tsunami/Storm Surge-Hazards Mitigation of Concrete Girder Bridges

Haibin Zhang, PhD
Associate Professor, School of Civil Engineering and Architecture, Hainan University
Research Consultant, Department of Civil, Architectural, and Environmental Engineering, Missouri University of Science and Technology

Genda Chen, PhD, PE, F.ASCE
Professor and Robert W. Abbett Distinguished Chair in Civil Engineering
Department of Civil, Architectural, and Environmental Engineering
Missouri University of Science and Technology

Riti Tie
Graduate Research Assistant
School of Civil Engineering and Architecture
Hainan University

Xinzhe Yuan, PhD
Graduate Research Assistant
Department of Civil, Architectural, and Environmental Engineering
Missouri University of Science and Technology

2024

A Cooperative Research Project sponsored by U.S. Department of Transportation- Office of the Assistant Secretary for Research and Technology

SMART Shear Keys for Tsunami/Storm Surge-Hazards Mitigation of Concrete Girder Bridges

Haibin Zhang, Ph.D.
Associate Professor
School of Civil Engineering and Architecture
Hainan University
(Formerly Research Consultant in the Department of Civil, Architectural, and Environmental Engineering, Missouri University of Science and Technology)

Genda Chen, Ph.D., P.E., F.ASCE
Professor and Robert W. Abbett Distinguished Chair in Civil Engineering
Department of Civil, Architectural, and Environmental Engineering
Director of the Center for Intelligent Infrastructure
Missouri University of Science and Technology

Riti Tie
Graduate Research Assistant
School of Civil Engineering and Architecture
Hainan University

Xinzhe Yuan, Ph.D.
Graduate Research Assistant
Department of Civil, Architectural, and Environmental Engineering
Missouri University of Science and Technology

A Report on Research Sponsored by

Mid-America Transportation Center

University of Nebraska–Lincoln

June 14, 2024

Technical Report Documentation Page

1. Report No. 25-1121-0005-132-4	2. Government Accession No.	3. Recipient's Catalog No.
4. Title and Subtitle SMART Shear Keys for Tsunami/Storm Surge-Hazards Mitigation of Concrete Girder Bridges		5. Report Date September 2024
		6. Performing Organization Code
7. Author(s) Haibin Zhang, Riti Tie, Genda Chen, and Xinzhe Yuan		8. Performing Organization Report No. 25-1121-0005-132-4
9. Performing Organization Name and Address Center for Intelligent Infrastructure Department of Civil, Architectural, and Environmental Engineering Missouri University of Science and Technology 500 W. 16th St. Rolla, MO 65409-0810		10. Work Unit No. (TRAIS)
		11. Contract or Grant No. 69A3551747107
12. Sponsoring Agency Name and Address Office of the Assistant Secretary for Research and Technology 1200 New Jersey Ave., SE Washington, D.C. 20590		13. Type of Report and Period Covered Final Report January 1, 2012, - June 30, 2024
		14. Sponsoring Agency Code MATC TRB RiP No. 91994-108

15. Supplementary Notes
This work was sponsored by the U.S. Department of Transportation under the Auspices of Mid-America Transportation Center.

16. Abstract

Bridges have recently been exposed to an increasing number of natural hazards such as earthquakes and tsunamis. These extreme events have resulted in transverse offsets, overturning moments, and even dropping-off of superstructures due to their weak connection to substructures. These outcomes are potentially prevented or mitigated by developing and deploying sliding, modular, adaptive, replaceable, and two-dimensional (SMART) shear keys as fuse elements between superstructures and substructures. The novelty of SMART shear keys is to enable an adaptive control of both the force and displacement of bridges under different types of loads. In this study, the performance of SMART shear keys under tsunami loading was investigated through a 1/5-scale six-girder concrete bridge model. Four levels of tsunami-like solitary waves 0.27~ 0.72 m in height were generated in the large wave flume and applied on the reinforced concrete bridge. To evaluate the performance of the shear keys, the dynamic responses of the bridge model were measured from accelerometers, load cells, and displacement sensors. The shear keys were prestressed to 0~200 MPa to represent flexible, medium, and fixed superstructure-substructure connections, respectively. The test results indicated that the residual displacements of the SMART shear keys were less than 1 mm in the vertical direction and zero in the horizontal direction. The energy dissipated by the SMART shear keys was up to 32.5% of the input energy that the bridge received from the tsunami loading. The natural frequency and energy dissipation of the bridge were respectively modified up to 18% and 14.2% by changing the prestress level of the SMART shear keys from 0 to 200 MPa.

17. ORCID No. of each Researcher Haibin Zhang: 0000-0003-4318-8202 Genda Chen: 0000-0002-0658-4356 Xinzhe Yuan: 0000-0003-4567-5362	18. Distribution Statement		
19. Security Classif. (of this report) Unclassified	20. Security Classif. (of this page) Unclassified	21. No. of Pages 60	22. Price

Table of Contents

List of Figures

List of Tables

Acknowledgments

The authors appreciate strong support provided by laboratory technicians in the Department of Civil, Architectural, and Environmental Engineering at Missouri University of Science and Technology. They would also like to thank Ms. Rebekah Miller and Dr. Tim Maddux for their assistance during test setup and data acquisition. They would like to thank Dr. Pedro Lomonaco for his support and assistance in setting up large-flume tests at Oregon State University and Dr. Christopher Higgins for his input and multi-girder bridge model made available during the laboratory tests. Thanks are also due to graduate students and post-doctoral fellows supervised by Dr. Genda Chen for their support during the laboratory tests.

Disclaimer

The contents of this report reflect the views of the authors, who are responsible for the facts and the accuracy of the information presented herein. This document is disseminated in the interest of information exchange. The report is funded, partially or entirely, by a grant from the U.S. Department of Transportation's University Transportation Centers Program. However, the U.S. Government assumes no liability for the contents or use thereof.

Executive Summary

Bridges have recently been exposed to an increasing number of natural hazards such as earthquakes and tsunamis. These extreme events have resulted in transverse offsets, overturning moments, and even dropping-off of superstructures due to their weak connection to substructures. These outcomes are potentially prevented or mitigated by developing and deploying sliding, modular, adaptive, replaceable, and two-dimensional (SMART) shear keys as fuse elements between superstructures and substructures. The novelty of SMART shear keys is to enable an adaptive control of both the force and displacement of bridges under different types of loads. In this study, the performance of SMART shear keys under tsunami loading was investigated through a 1/5-scale six-girder concrete bridge model. Four levels of tsunami-like solitary waves 0.27~ 0.72 m in height were generated in the large wave flume and applied on the reinforced concrete bridge. To evaluate the performance of the shear keys, the dynamic responses of the bridge model were measured from accelerometers, load cells, and displacement sensors. The shear keys were prestressed to 0~200 MPa to represent flexible, medium, and fixed superstructure-substructure connections, respectively. The test results indicated that the residual displacements of the SMART shear keys were less than 1 mm in the vertical direction and zero in the horizontal direction. The energy dissipated by the SMART shear keys was up to 32.5% of the input energy that the bridge received from the tsunami loading. The natural frequency and energy dissipation of the bridge were respectively modified up to 18% and 14.2% by changing the prestress level of the SMART shear keys from 0 to 200 MPa.

Chapter 1 Introduction

1.1 Objective

Bridges are essential components of modern infrastructure, crucial for enabling mobility and facilitating the flow of goods. However, as natural disasters occur more frequently, the safety of bridges has emerged as a significant concern. Extreme events such as earthquakes and tsunamis often result in unpredictable damage to bridge structures, including lateral displacement and overturning moments. These issues not only impact the normal use of bridges but also pose threats to vehicle safety. Additionally, connections between the superstructure and substructure are weak points in bridge structures, significantly affecting their safety. If the upper structure of a bridge were to detach, serious consequences could follow. In recent years, researchers have introduced the notion of shear keys. These shear keys serve as sacrificial elements, directing sliding shear failure to safeguard foundation piers or cap beams from harm. In cases of earthquakes, tsunamis, and similar disasters, if sacrificial smart shear keys fail, they can be substituted with new ones to enhance readiness for future seismic and tsunami occurrences. To limit lateral displacement of bridge decks caused by seismic forces, engineers employ external and/or internal sacrificial shear keys in girder bridges. However, due to existing gaps in information, more detailed research is necessary. Firstly, the specific effects of prestress levels, friction coefficients, and loading paths on the performance of shear keys are not yet clear. Secondly, exhaustive examination of shear keys' energy dissipation ability remains incomplete under both repeated and monotonic loading

scenarios. Furthermore, there is scarce information available on the performance of shear keys under different seismic loading conditions.

1.2 Literature review on splicing structure for shear keys

1.2.1 Design concept and category

The shear keys play a vital role in bridge structures by regulating the lateral displacement of the bridge deck when subjected to seismic activity or other external forces. Shear keys are generally located between the superstructure (e.g., girders) and the substructure (e.g., piers or abutments) of a bridge and serve to effectively connect the two parts and transfer loads. According to the current California Bridge Design Code (CALTRANS, 2019), the transfer of lateral seismic forces to the abutment piles is controlled by the design of the shear key such that the maximum shear capacity of the shear key does not exceed the lesser of 30 percent of the dead load vertical reaction at the abutment and 75 percent of the total shear capacity of the pile plus the shear capacity of one of the wing-walls. In this design approach, the sacrificial shear keys are anticipated to undergo failure initially, causing minimal and repairable damage to the abutment walls.

Shear keys can be classified into two types based on their location: external shear keys and internal shear keys, as shown in Figure 1.1 and Figure 1.2.

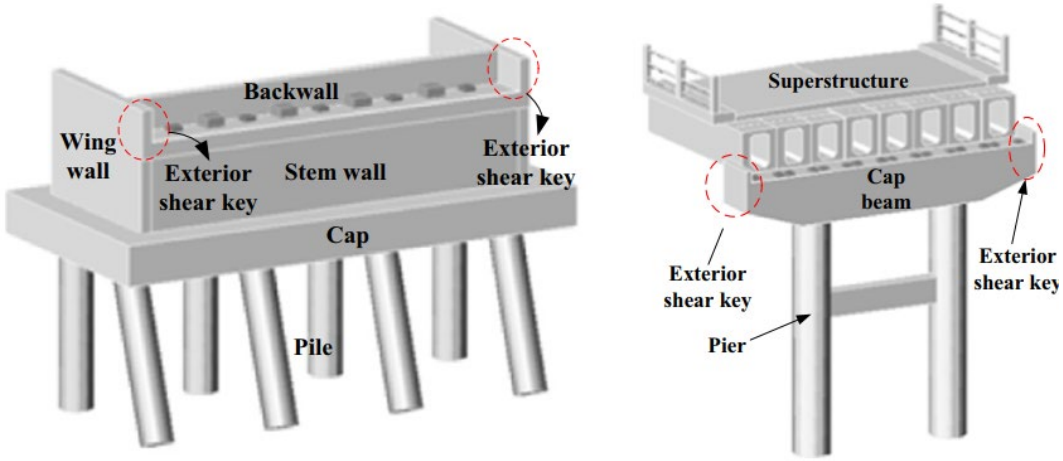

(a) Abutment (b) Cap beam

Figure 1.1 Exterior shear key located at (a) Abutment and (b) Cap beam (Han et al., 2017)

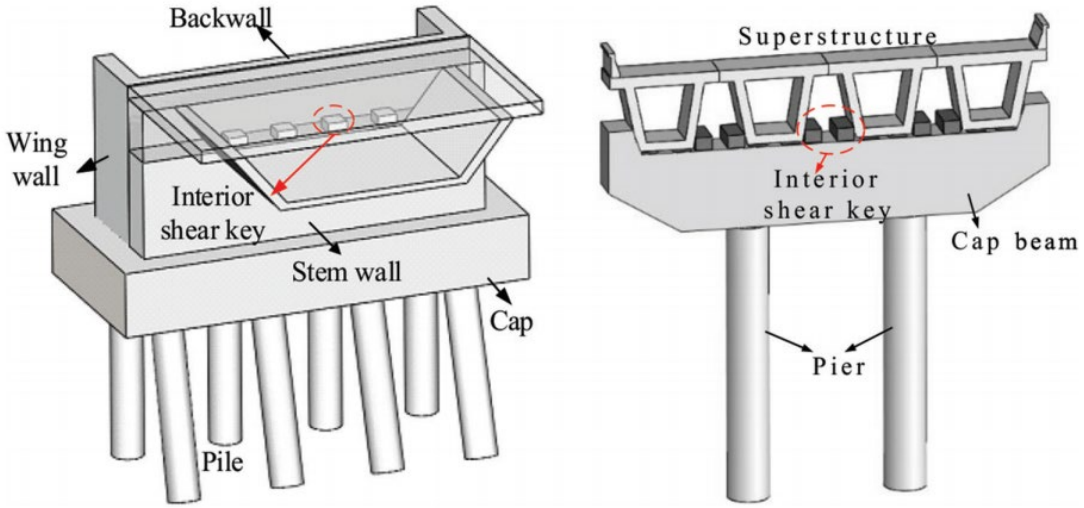

(a) Abutment (b) Cap beam

Figure 1.2 Interior shear key located at (a) Abutment and (b) Cap beam (Han et al., 2018)

The interface disparity between the shear key and abutment/cap beam delineates two classifications: monolithic shear keys and isolated shear keys, as shown in Figure 1.3 and Figure 1.4.

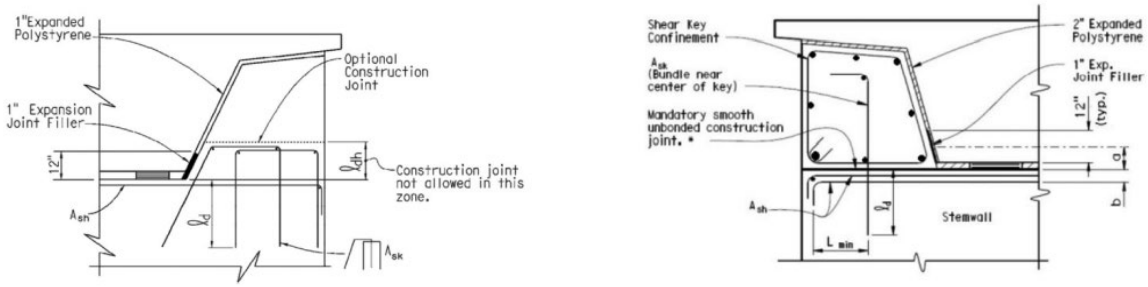

(a) Monolithic shear key (b) Isolated shear key

Figure 1.3 Exterior (a) monolithic and (b) isolated shear key (Kottari et al. (2020)

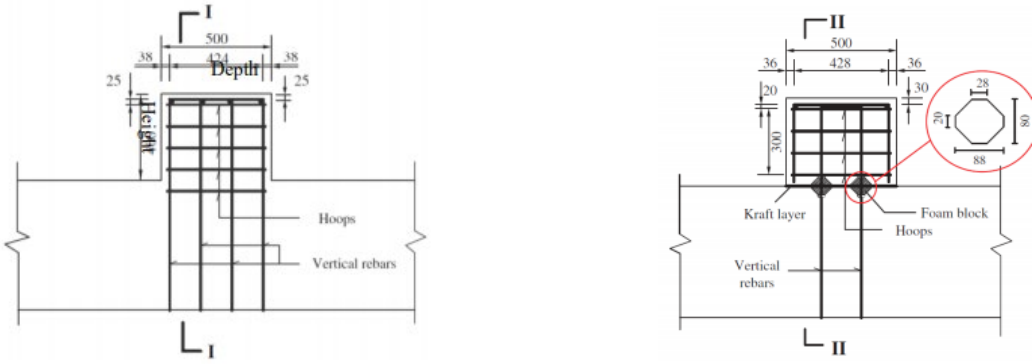

(a) Monolithic shear key (b) Isolated shear key

Figure 1.4 Interior (a) monolithic and (b) isolated shear key (Han et al., 2018)

1.2.1.1 Exterior sacrificial shear keys

Megally et al. (2001) presented an experimental program that investigated the evaluation of the performance of external sacrificial shear keys for six bridge abutments under simulated seismic loading. Variables in the external shear key tests included the back and wing walls, the use of different key details, and the post-tensioning of the abutment pole walls. Based on the test results it was shown that the piles and wing walls of the abutments were at high risk of significant damage. Since significant damage to the abutment walls or the piles beneath them is undesirable because it makes post-earthquake repairs difficult and may

require reconstruction of the abutment walls, the use of shear keys as a means of controlling damage to the piles is practically non-conservative for the design of sacrificial shear keys. A two-spring component hysteresis analysis model was developed based on experimental results, and mathematical rules describing the hysteresis model were given. The analysis shows that the shear friction model used in Caltrans design specifications is nonconservative for the design of sacrificial shear keys, which may lead to overloading of bearing and support piles.

Bozorgzadeh et al. (2006) conducted an experimental research program at the University of California, San Diego to better understand the seismic performance of sacrificial external shear keys for bridge abutments according to Caltrans specifications by designing and constructing ten external shear keys at a scale of 1:2.5, with different types of connections at the shear-key-abutment and reinforcement interfaces. The primary objective of the research program was to reassess the validity of the design equations in order to estimate the capacity of the shear keys within a capacity design framework. A secondary objective was to provide data to develop analytical models that could be used to accurately estimate shear key capacity, and finally, to provide appropriate reinforcement details and preparation of construction joint faces at the shear keys-rod wall interface to allow the shear keys to function as a structural lead. The experimental results indicate that smooth construction joints should be used to allow sliding shear damage to occur at the shear key-abutment rod wall interface. In addition, a mechanistic model for the evaluation of the sliding shear damage

shear key capacity was developed for assessing the ability of exterior shear keys to slide shear damage.

An experimental evaluation was carried out by Silva et al. (2009) to study the as-built sacrificial external shear keys for various construction joint types and to analyze their load-displacement response at peak and post-peak phases under cyclic loading. Based on the experimental results, a hysteretic model for a two-spring component with gap and strength degradation was developed. This model accurately replicated the cyclic response of shear keys, including their stiffness and capacity degradation, which were caused by the loss of aggregate interlocking and the fracture of the reinforcement.

Han et al. (2017) presented an experimental study on the seismic performance of reinforced concrete (RC) sacrificial exterior shear keys, considering the effects of reinforcement ratio and the type of construction joint. Three failure modes of the shear key under reversed loads were outlined, with the introduction of two analytical models for forecasting the force-displacement backbone curve. These models demonstrated a strong concordance with experimental findings.

Kottari et al. (2020) introduced a novel design approach aimed at mitigating the abrupt and unpredictable diagonal shear failure often observed in conventional monolithic exterior shear keys. This method facilitates a more controlled failure mechanism, where the horizontal sliding of the shear key takes precedence over the diagonal cracking of the stem wall. The experimental results have confirmed the validity of the analytical formulas and design methodology.

1.2.1.2 Interior sacrificial shear keys

Megally et al. (2001) examined how seven interior shear keys responded to seismic activity. The experiment explored various loading protocol, geometric aspect ratios, and reinforcement ratios of the shear keys. The findings indicated that the performance of interior shear keys is minimally impacted by factors such as load history, aspect ratio, and reinforcement ratio. However, the aspect ratio influenced the deterioration of cyclic friction loading and observed levels of damage. Greater aspect ratios resulted in reduced degradation of the friction load.

Han et al. (2018, 2020) primarily explored the seismic behavior, damage modes, and load transfer mechanisms of internal shear keys subjected to cyclic transverse loading reversal. They then implemented suitable construction fuses at the interface between the shear key and the cap beam to guarantee their effectiveness as structural fuses. Furthermore, a computational model is formulated for analyzing the load-displacement behavior of shear keys in various types of structural fuses, aiming to precisely forecast their response. The seismic capacity of six interior shear key specimens was assessed using varying main parameters including the number and ratio of vertical bars, hoop ratio, shear span ratio, loading height, and presence of construction joints. Three distinct failure modes were detected in the interior shear key specimens during the experiments. Additionally, distinct analytical frameworks were devised for the three failure modes, along with an empirical formula, to gauge the seismic capacity of the specimens. Upon comparison with the

experimental data, these refined approaches demonstrated superior accuracy in predicting load-carrying capacity compared to traditional analytical models.

1.2.2 Failure mode of splicing structure for shear key

1.2.2.1 Diagonal shear failure

This form of failure commonly occurs within monolithic construction joints, primarily dictated by the collective resistance provided by the vertical reinforcements and hoops crossing the inclined cracks as shown in Figure 1.5. The failure of interior shear keys primarily occurs within the shear key itself. In contrast, for exterior shear keys, cracks tend to propagate diagonally towards the base of the stem wall. The failure mechanism of external shear keys does not involve sacrificial components, and significant abutment damage can be anticipated in the event of a major earthquake. Hence, it is advisable to steer clear of this failure mode for external shear keys.

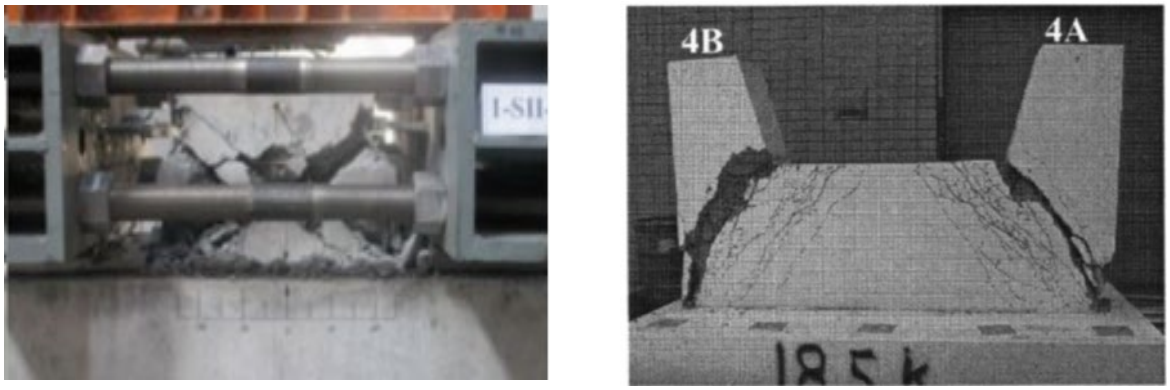

(a) Interior (Han *et al*., 2018) (b) Exterior (Bozorgzadeh *et al*., 2006)

Figure 1.5 Diagonal shear failure mode of shear key

1.2.2.2 Sliding shear failure mode of shear key

The sliding shear failure mode is distinguished by the lateral movement of the shear keys along the interface of the shear keys and the abutment stem wall. When subjected to minor displacement, numerous diagonal cracks suddenly emerge near the point of loading. Subsequently, additional diagonal cracks manifest on the loading side and progress towards the base of the specimen. As the load escalates, following the specimen's peak load, its bearing capacity diminishes due to concrete spalling. Eventually, the overlay concrete fractures, accompanied by interfacial cracks, followed by concrete spalling and expansion along the entire length of the specimen, leading to the fracture of some vertical shear key reinforcements, as shown in Figure 1.6(a) and (b), respectively.

(a) Interior (Han *et al*., 2018) (b) Exterior (Megally *et al*., 2001)

Figure 1.6 Sliding shear failure mode of shear key

Xiao et al. (2022) performed two series of push-out experiments on shear keys embedded in UHPC, where they analyzed damage patterns, load-strain relationships, and other relevant data. The key mechanical parameters of the shear keys were assessed, and a

comparison was drawn between their mechanical behavior in UHPC and regular concrete. Furthermore, the suitability of an established formula for calculating the load capacity of shear keys was examined. During loading, cracks initially formed in the middle of the outer surface of the UHPC blocks. As the load increased, these cracks propagated both upwards and downwards at varying rates of progression, while the widths of the cracks gradually widened. Concurrently, steel fibers were either pulled out or detached from the UHPC. However, no new cracks emerged during this period. Throughout, there was a continual increase in relative slip between the steel and the UHPC. In the later stages of loading, this relative slip escalated rapidly, showcasing commendable ductility in the specimen. The ultimate damage observed was the shearing of the penetrating bars, while the UHPC itself remained intact aside from the outer vertical cracks, which could effectively serve as a wrapping mechanism for the shear keys.

Figure 1.7 Specimen surface damage pattern (Xiao et al. 2022)

1.2.2.3 Shear friction failure

The shear key acted as a sacrificial component by generating sliding shear friction, thus safeguarding the abutment stem wall from damage. After attaining peak strength, horizontal cracks emerged at the base of the sample, accompanied by steep softening due to the failure of the concrete shear keys at the construction joint in this component. As testing progressed in both experimental units, notable sliding of the shear key occurred at the interface between the shear key and the abutment rod wall. There was a slight reduction in bearing capacity as the reinforcement elongated. The vertical reinforcement within the shear key ruptured under increased displacement, resulting in the failure of the shear key. To address this, the shear keys can be extracted, and new vertical reinforcement can be installed by drilling vertical holes. Subsequently, the holes would be filled with grout and new shear keys would be cast.

(c) Interior (Han *et al*., 2018)

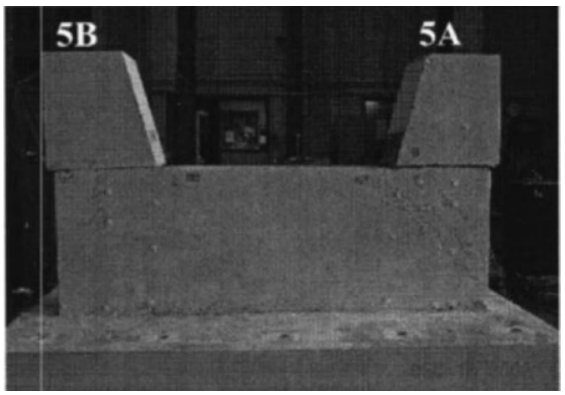

(d) Exterior (Bozorgzadeh *et al*., 2006)

Figure 1.8 Sliding friction failure mode of shear key

According to Yuan and Chen (2018), a smart shear key is designed to have a sliding friction failure mode. As a result, the bent cap or abutment will remain undamaged as the shear key absorbs the impact. Following an earthquake, the shear key can be easily replaced. The typical failure mode is presented in Figure 1.9.

Figure 1.9 Failure mode of friction failure mode (Yuan *et al*.,2018)

1.3 Experimental results of shear key

1.3.1 Experimental results of Exterior shear key

Bozorgzadeh et al. (2006) developed and built 10 shear keys at a 1:2.5 scale, modeled on a prototype bridge abutment design from Caltrans, and conducted five experimental series. The experimental study was on the shear performance and failure behaviors of shear key external bridge abutments under transverse forces. In the first test series, shear key 1A was

constructed without including an abutment back-wall or wing-walls. Conversely, in unit 1B, the abutment back-wall and wing-walls were constructed as a single, continuous structure along with the exterior shear key, as shown in Figure 1.10(a). In the second test series, the design of shear key 2A mirrored that of shear key 1A, as it was constructed on a hardened, smooth concrete surface of the bridge abutment stem wall. On the other hand, shear key 2B was engineered to exhibit a more pronounced flexural response, as shown in Figure 1.10(b). In the third Test Series, shear Keys 3A and 3B were designed similarly to shear key 2A but incorporated post-tensioning of the abutment stem wall in the transverse direction, relative to the longitudinal axis of the superstructure, as shown in Figure 1.10(c). In the last test series, the shear key was constructed differently in the two units. In unit 4A, the shear key was constructed integrally with the abutment stem wall, i.e. it was constructed as a single unit. In contrast, the shear key in unit 4B was cast separately and placed over rough joints, i.e. the shear key was added to the structure after the initial construction phase, as shown in Figure 1.10(d).

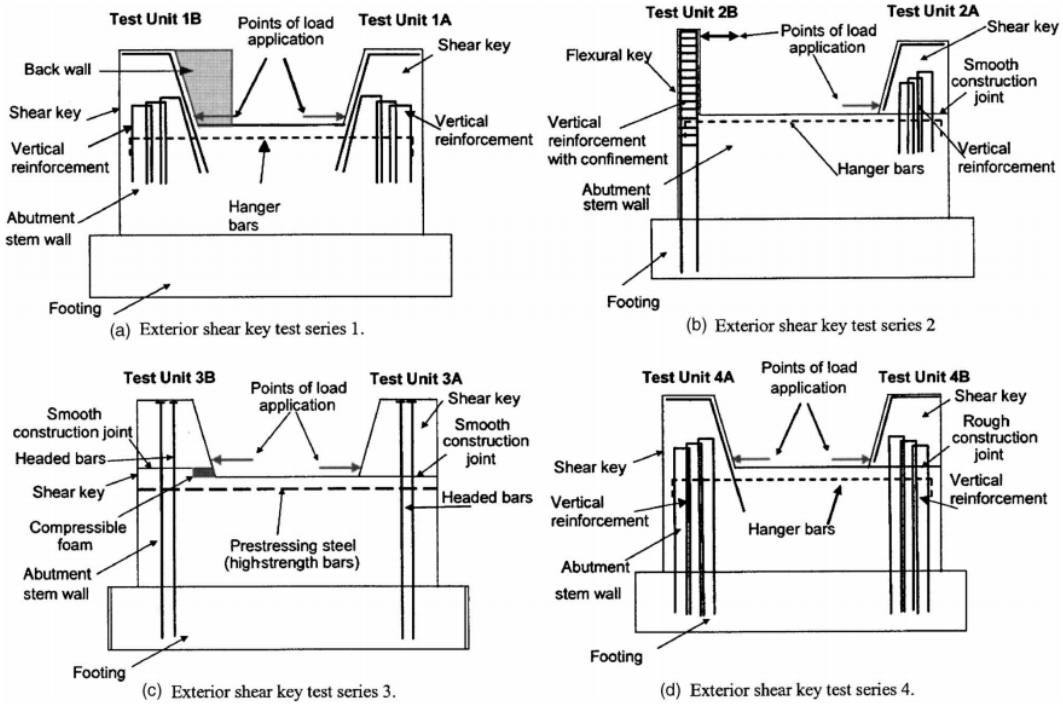

Figure 1.10 Exterior shear key series 1, 2, 3, and 4 (Bozorgzadeh et al., 2006)

The plotted data in Figure 1.11(a) illustrates the relationship between lateral force and lateral displacement as measured across shear Keys 1A, 1B, 2A, 4A, and 4B. It becomes evident from Figure 1.11(a) that integrating back- and wing-walls, constructed monolithically with the shear key, would notably enhance the shear key's capacity. Due to the smooth construction joint at the interface between unit 2A's shear key and stem wall, an initial horizontal crack emerged, gradually extending until it intersected the first row of vertical shear key reinforcement. As the test progressed, multiple inclined cracks manifested within the stem wall. The lack of adequate tie reinforcement within the abutment stem wall exacerbated the widening of diagonal cracks throughout the experiment. Remarkably, the collective behavior of shear keys 1A, 1B, 2A, 4A, and 4B closely mirrored one another, culminating in a definitive diagonal shear failure.

Shear key 2B, employing the flexural-dominated approach, demonstrated a flexural shear response during testing. The test of the flexural key revealed a ductile behavior, showcasing its capacity to withstand significant deformation. Notably, a flexural plastic hinge emerged at the interface between the shear key and the abutment stem wall. The force-displacement response of shear key 2B, depicted in Figure 1.11(b), underscores its robust performance. Even at a displacement ductility factor of 8, shear key 2B experienced only a minor loss in capacity, indicating the remarkable energy dissipation capabilities inherent in flexural shear keys. Overall, these findings highlight the effectiveness of flexural shear keys in withstanding structural forces while maintaining their integrity and dissipating energy efficiently.

The shear keys 3A and 3B depicted in Figure 1.11(c) exhibited a notable decline in capacity due to the rupture of several critical shear bars. However, as the experiment progressed, there were no further instances of bar rupture, resulting in a negligible alteration in the shear keys' capacity.

In Figure 1.11(d), the force-displacement responses of shear keys 5A and 5B are delineated. Following the attainment of maximum strength, this particular unit underwent a notable softening marked by the fracture of concrete keys at the construction joints. Subsequently, as the test progressed, both test units exhibited a gradual augmentation in load capacity attributed to the development of kinks in the shear-critical vertical reinforcement. However, at greater displacements, the vertical reinforcement of the shear keys succumbed to fracture, resulting in damage to the shear key structures. Notably, a discernible drop in load

carrying capacity was observed when the vertical reinforcement reached the yield point, approximately at 340 kN, as evident from Figure 1.11(d).

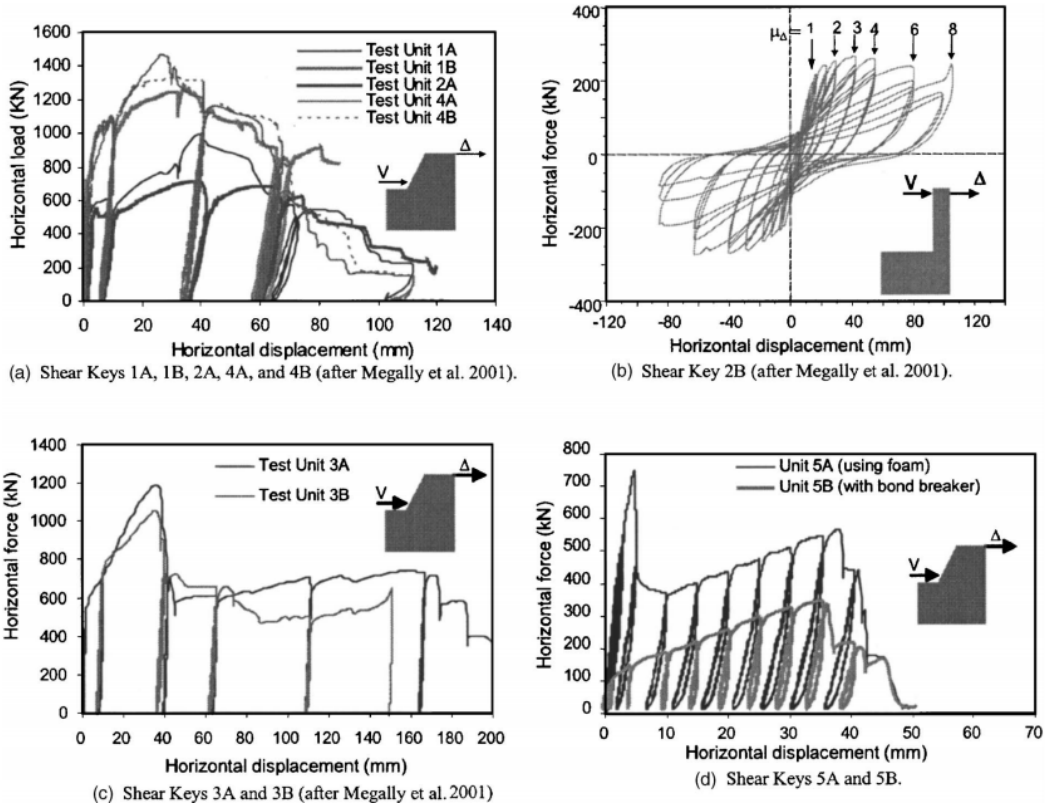

(a) Shear Keys 1A, 1B, 2A, 4A, and 4B (after Megally et al. 2001).
(b) Shear Key 2B (after Megally et al. 2001).
(c) Shear Keys 3A and 3B (after Megally et al. 2001)
(d) Shear Keys 5A and 5B.

Figure 1.11 Measured lateral force-displacement responses (Bozorgzadeh et al.,2006)

Based on these experimental results, a straightforward model has been developed for assessing the load-carrying capacity and performance of shear keys. This model is intended to be utilized in the design of sacrificial shear keys. The experimental results were compared with the analytical results, and it was concluded that the developed model for evaluating the load carrying capacity of the external shear keys is more consistent with the experimental results than the existing shear friction model. Figure 1.12 shows a schematic model based on the one proposed by Crisafulli et al. 2002. The model considers the deformed shape of the

reinforcement during the failure of shear keys. To accurately measure the angle of the kinked vertical bar, the fractured vertical bar was extracted from within the shear key and the bar wall. After reassembling the two fractured pieces, the kinked vertical bar appears as depicted in Figure 1.13.

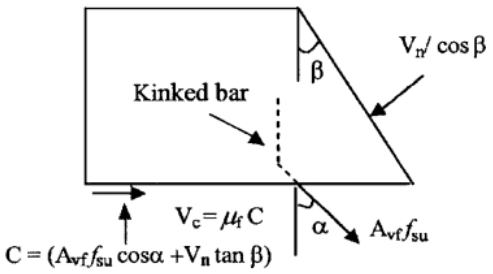

Figure 1.12 Mechanism model of exterior shear key in shear sliding failure (Bozorgzadeh et al.,2006)

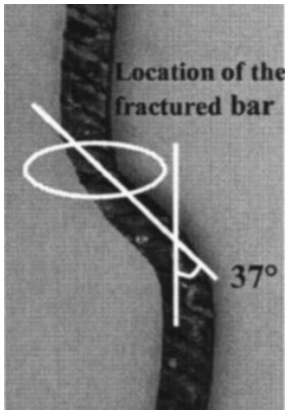

Figure 1.13 Fractured vertical bar in Shear Key (Bozorgzadeh et al.,2006)

Han et al. (2017) conducted an experimental study to investigate the seismic performance of reinforced concrete sacrificial exterior shear keys. Their research concentrated on how different reinforcement rates and types of construction joints affect the mechanical behavior of these shear keys. They developed two analytical models to characterize the force-displacement principal curves for shear keys experiencing sliding shear failure and sliding friction failure. The study involved testing ten shear key specimens under lateral reversed loading to evaluate the seismic behavior of sacrificial exterior shear keys in highway bridges. The ten exterior shear key specimens were split into two distinct groups.

The first group, comprising Specimens S1 to S6, had a monolithic construction at the interface between the shear key and the stem wall. The second group, including Specimens S7 to S10, featured a seismic resilient construction joint surface preparation at this interface.

Diagonal cracks manifested within specimens S1 and S2 once the displacement reached 1 mm during the second cycle. These cracks initiated from the interior of the shear key and gradually propagated outward, ultimately leading to the shear key's structural failure. The failure progression of specimen S1 is visually depicted in Figure 1.14.

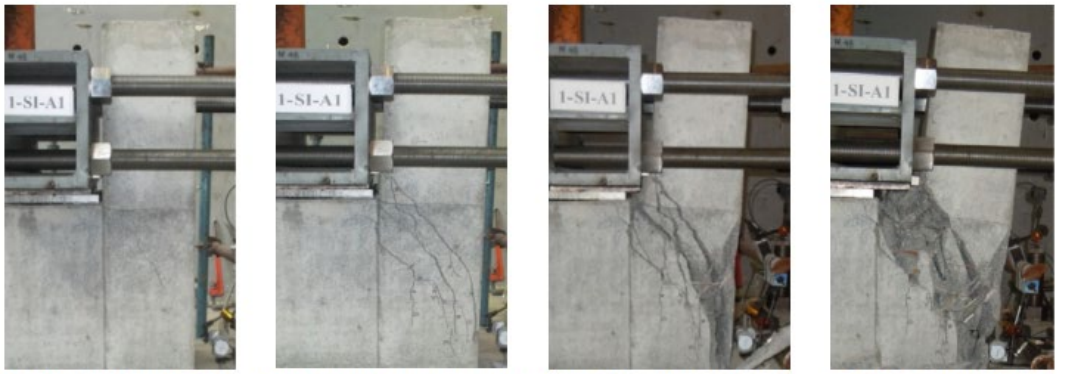

(a) Initial cracking (at the displacement of 1mm) (b) Cracks propagating (at the displacement of 26mm) (c) Cracks widening (at the displacement of 80mm) (d) End of test (at the displacement of 180mm)

Figure 1.14 Damage process of Specimen S1 (Han et al., 2017)

Horizontal cracks near the shear key-stem wall interface emerged in specimens S3 to S6 during the initial cycle. Subsequently, a proliferation of horizontal cracks at the interface and inclined cracks in the drywall became apparent as the testing progressed. The progression of damage in specimen S3 is illustrated in Figure 1.15.

(a) Initial cracking (at the displacement of 1mm) (b) Cracks propagating (at the displacement of 5mm) (c) Cracks widening (at the displacement of 25mm) (d) End of test (at the displacement of 175mm)

Figure 1.15 Damage process of Specimen S3 (Bozorgzadeh et al.,2006)

During the second cycle, specimens S7 to S10 exhibited the emergence of horizontal cracks originating from within the shear keys at the interface with the stem wall. As the testing progressed, the protective layer of concrete gradually spalled off, leading to the shear keys sliding against the drywall. Remarkably, even upon reaching the final failure state, the drywall maintained its integrity with only minor instances of concrete cover spalling. Figure 1.16 illustrates the failure process of specimen S9.

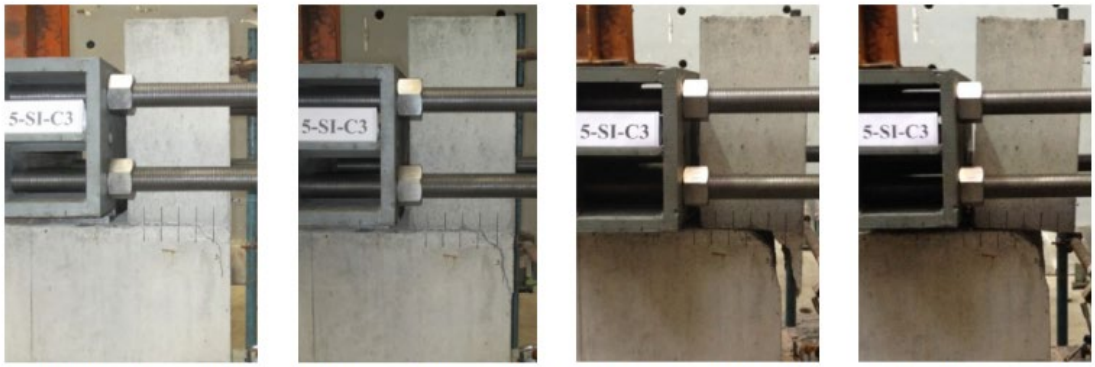

(a) Initial cracking (at the displacement of 1mm) (b) Cover spalling (at the displacement of 3mm) (c) Shear key sliding (at the displacement of 80mm) (d) End of test (at the displacement of 110mm)

Figure 1.16 Damage process of Specimen S9 (Han et al., 2017)

Specimens S1 and S2 exhibit diagonal tension failure in the shear key test, as depicted in Figure 1.17(a). Sliding shear failure, depicted in Figure 1.17(b), characterizes Specimens S3 through S6. Their capacity to bear loads predominantly stems from the combined resistance offered by the vertical reinforcement and the concrete. The specimens labeled S7 to S10 exhibit resilient construction joints characterized by failure due to sliding friction. In these cases, the bearing capacity primarily stems from the combined resistance offered by the vertical reinforcement and the frictional forces occurring at the interface between the shear key and the stem wall, as depicted in Figure 1.17(c). The results revealed that shear key specimens featuring monolithic construction joints experienced both diagonal shear failure and sliding shear failure. The extent of failure was contingent upon the proportion between the total cross-sectional area of horizontal reinforcement and that of vertical reinforcement (A_{sh}/A_{sv}). In contrast, shear key specimens incorporating resilient construction joints suffered failure primarily through sliding friction, resulting in lesser damage to the stem wall.

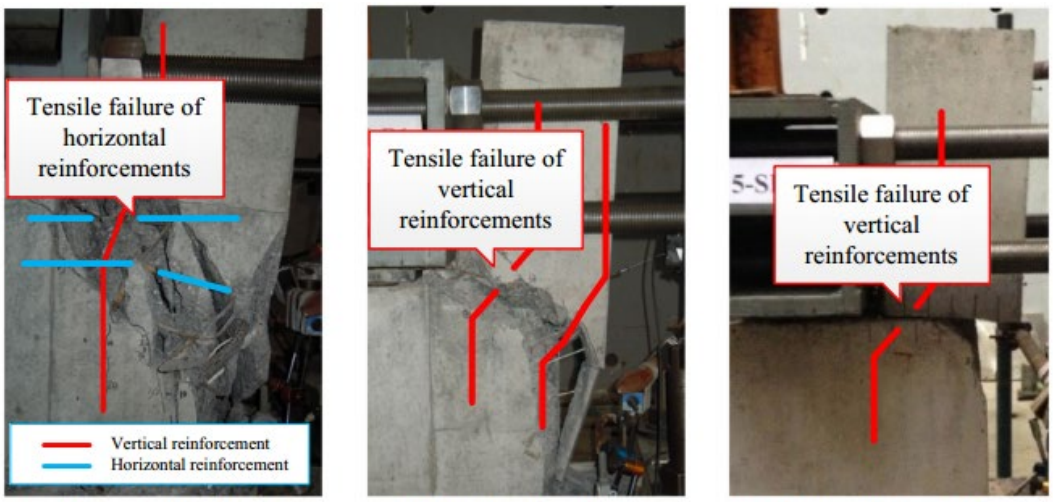

(a) Diagonal shear failure (b) Sliding shear failure (c) Sliding friction failure

Figure 1.17 Failure modes observed during the tests (Han et al., 2017)

Figure 1.18 displays the hysteresis curves depicting the lateral load versus displacement for three shear key specimens, each subjected to different damage modes. Given that the loading and unloading stiffnesses of all specimens are essentially identical, the curve depicted in Figure 1.19 provides a qualitative means to assess and compare the seismic performance of the shear key specimens. For specimens featuring monolithic structural construction joints, a reduction in the vertical reinforcement ratio resulted in a lower maximum load-carrying capacity and corresponding displacements. Additionally, as the ratio of Ash to A_{sv} increased, the peak lateral displacement decreased. For specimens with resilient structural construction joints, a reduction in the vertical reinforcement ratio leads to a decrease in maximum load-carrying capacity and an increase in the extent of the descending branch. Although these specimens exhibit a higher displacement ductility factor compared to those with monolithic structural construction joints, their maximum lateral force is lower.

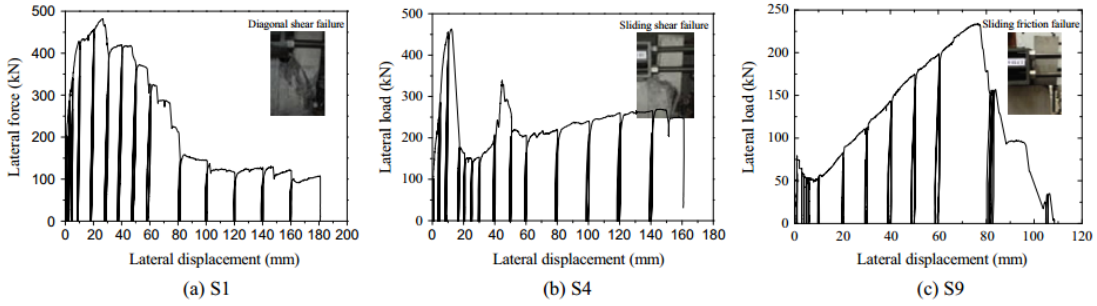

(a) S1 (b) S4 (c) S9

Figure 1.18 Measured load-displacement curves of typical specimens with different failure modes (Han et al., 2017)

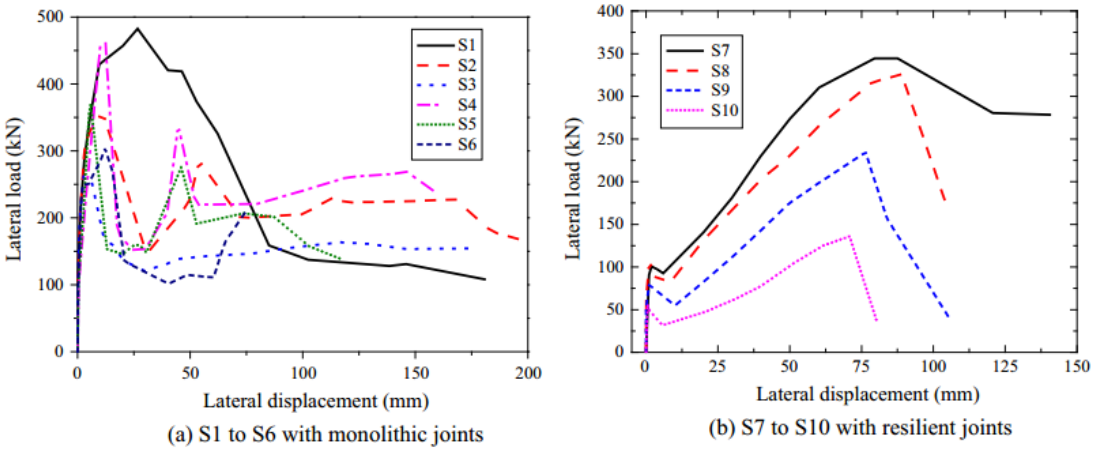

Figure 1.19 Lateral load-displacement envelop curves of specimens (Han et al., 2017)

1.3.2 Experimental results of Interior shear key

Han et al. (2018, 2020) conducted tests on the seismic capacity of six internal shear key specimens. The experimental results revealed three distinct failure modes: diagonal tension failure, sliding shear failure, and sliding friction failure. Strain gauges were installed on the vertical reinforcement to observe the strain distribution, as illustrated in Figure 1.20. In the experiment, S1 and S3 feature identical quantities of vertical reinforcement but vary in their shear-span ratios. Conversely, S3 and S4 share the same shear-span ratio, differing instead in the amount of vertical reinforcement used. Figure 1.20(a) shows the strain distribution in the vertical reinforcement of S1. The yielding strain was achieved solely in the upper part of the reinforcements. In S3, the strain distribution depicted in Figure 1.20(b) indicates the reinforcing bars yielding at Z = 2, a characteristic of the specimen exhibiting a sliding shear failure mode. In S4, Figure 1.20(c) depicts the strain distribution of vertical reinforcement, wherein the vertical reinforcements of the shear key yielded at Z = 1 and 2.

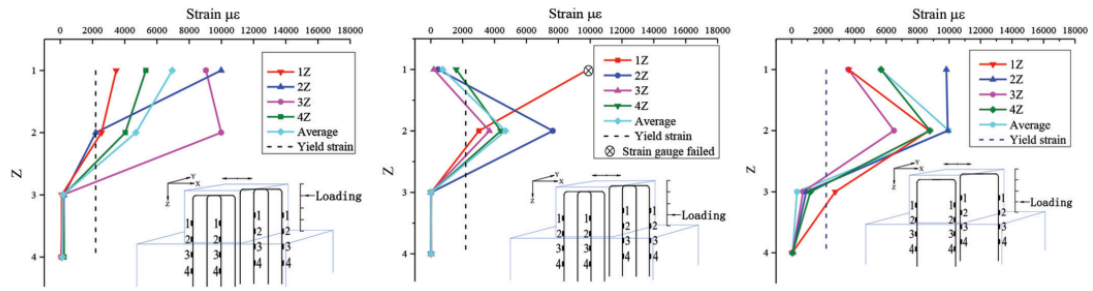

Figure 1.20 Vertical reinforcement bar strain distribution (Han et al.,2018)

Table 1.1 provides the maximum load capacity, along with the displacement at peak load and the displacement ductility factor for each specimen. As the shear-to-span ratio decreases, there is a noticeable increase in the maximum bearing capacity of the integral shear keys, as indicated by the experimental results. As the vertical reinforcement ratio increases, so does the maximum load carrying capacity of the elastic specimens. The load carrying capacity is greater in the monolithic construction joint specimens compared to their resilient counterparts, albeit at the expense of reduced displacement ductility. Furthermore, the resilient internal shear keys demonstrates commendable ductility characteristics.

Table 1.1 Maximum load-carrying and displacement ductility

Specimen	Shear span ratio α	Vertical reinforcement ratio, %	Maximum capacity, kip (KN)	Displacement, in. (mm)	Displacement ductility factor
S1	0.6	0.52	120.95(538)	0.20(5.1)	2
S2	0.4	0.52	120.95(538)	0.12(3.0)	2
S3	0.2	0.52	120.95(538)	0.15(3.8)	2
S4	0.2	0.26	120.95(538)	1.60(40.7)	44
S5	0.2	0.52	58.23(259)	1.94(49.4)	30
S6	0.2	0.78	58.23(259)	1.51(38.4)	38

Figure 1.21 shows the load-displacement hysteresis curve responses of S1, S2, S3, S4, S5, and S6. By connecting the peak points of each hysteresis curve, the envelope response, as depicted in Figure 1.22, is obtained. The force-displacement envelope response of the interior shear key specimens can be adequately predicted by both analytical models when compared with experimental data.

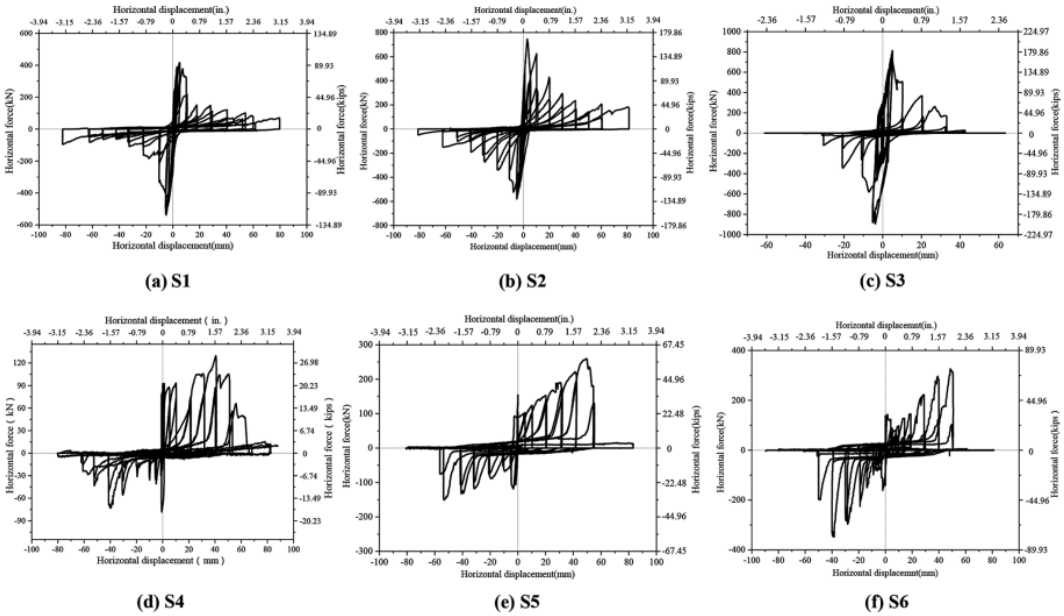

Figure 1.21 Hysteretic curves of specimen with different construction joint types (Han et al., 2018)

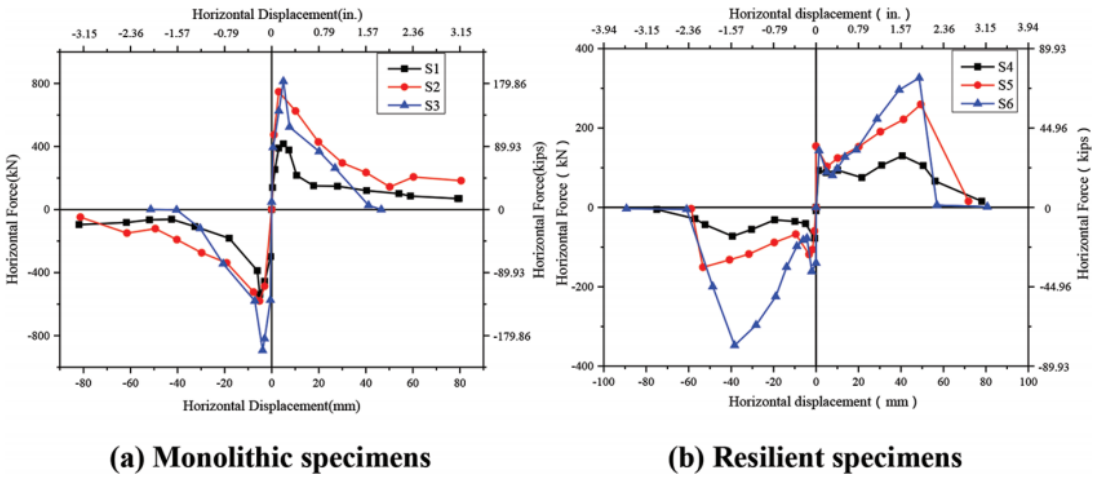

Figure 1.22 Envelope curves of specimens (Han et al., 2018)

Li et al. (2018, 2020) investigated the seismic damping performance of a slip-plate rubber bearing system with a shear key. The study resulted in the proposal of a design calculation method and establishment of a restoring force model for the shear key. By combining the model with the numerical analysis method, a simple calculation formula was given. Six seismic waves were selected, as shown in Figure 1.23, and OpenSees was used to establish a nonlinear dynamic model of the bridge and perform a time course analysis. The results show that: the number of shear keys has a significant effect on the damping effect of the slip-plate rubber bearing, and the reasonable arrangement of the shear keys can effectively prevent the main beam from slipping under the normal earthquake, and significantly reduce the post-earthquake residual displacement and the internal force of the bridge abutment under the rare earthquakes.

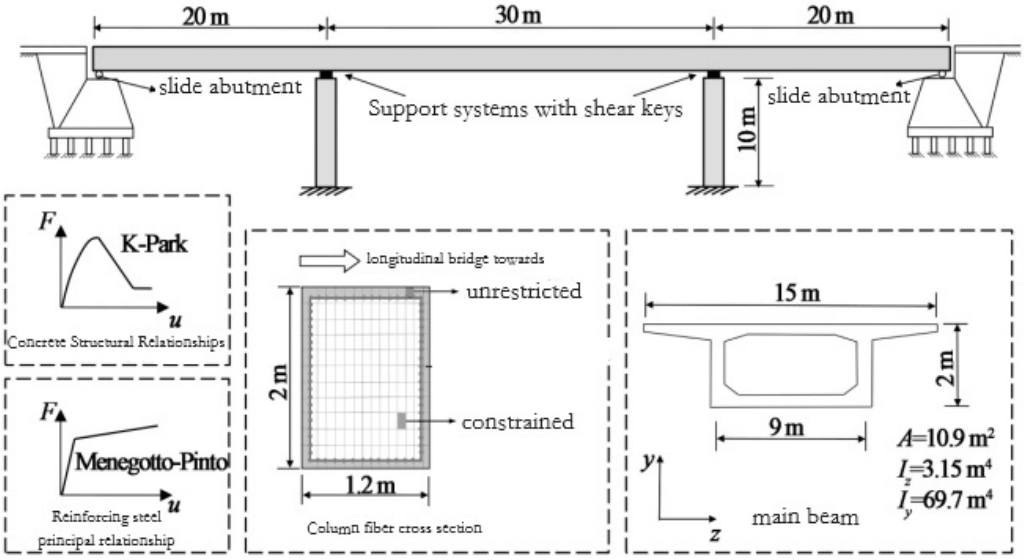

Figure 1.23 Schematic of the continuous bridge (Han et al., 2018)

Chapter 2 Design of Experiment

2.1 Specimen details

2.1.1 SMART shear key

As shown in Figure 2.1, the SMART shear key consists of module I, module II, and module III. Module I and module II are linked by two horizontally oriented high strength bolts. Similarly, module II and module III are linked by two vertically oriented high strength bolts. The vertical contact surfaces of modules I-II and the horizontal contact surfaces of modules II-III are not perpendicular to their respective pins at a small angle (5°) to control the clamping force required in case of excessive movement. Module III is firmly fixed by embedding it within the structure of the main beam. The lateral (and vertical) sliding interface experiences keys-slip behaviors as observed in similar designs (Kottariet al. 2017).

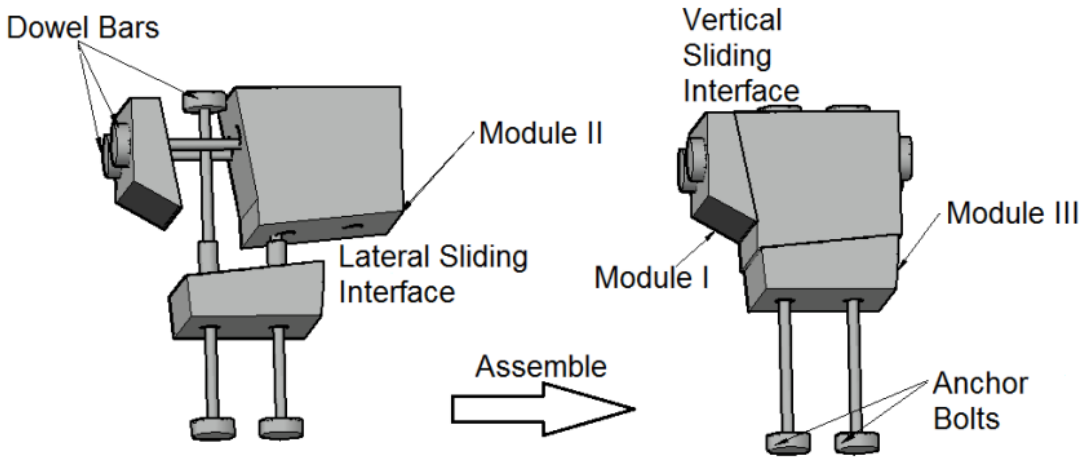

Figure 2.1 Assembling schematic of Smart shear keys

2.1.2 Working Principle of SMART shear key

The working principle of the shear key is demonstrated in Figure 2.2. In bridge applications, module III is embedded into a cap beam, and module II and module I are against an RC or steel girder horizontally and vertically. As the horizontal tsunami loading begins to increase, module II initially sticks to module III. When their static friction is exceeded, module II begins to slide against Module III and their kinetic friction increases with increasing loading. The dowel bars can be prestressed to increase the clamping force for friction controllability. Under excessive dynamic loading, the dowel bars will yield and produce dowel action to limit further displacement of the bridge superstructure.

Since the SMART shear key works in the same way both vertically and horizontally, module II and module III are considered in the following derivation for horizontal load capacity of the shear key. As depicted in Figure 2.2, the force balances in horizontal and vertical directions yield the following two equations.

$$V_h = nA_s f_y \sin\alpha + \mu_f N \cos\beta + N \sin\beta \quad (1)$$

$$N \cos\beta = \mu_f N \sin\beta + nA_s f_y \cos\alpha \quad (2)$$

where $sin\,\alpha = \frac{\sqrt{\varepsilon_h^2+2\varepsilon_h}}{1+\varepsilon_h}$ and $cos\,\alpha = \frac{1}{1+\varepsilon_h}$, α is the angle between the original and deformed dowel bar, ε_h is the strain in the dowel bar, V_h is the horizontal load applied on the shear key, n is the total number of dowel bars, A_s is the cross-sectional area of the dowel bar, f_y is the yield strength of the dowel bar, N is the clamped force at the module II-III interface, which is

the normal force applied on the interface, $\mu_f = \tan \gamma_f$ is the coefficient of kinetic friction between the two modules, and γ_f is the angle of friction.

Substituting Equation (2) into (1) gives the load capacity of the shear key.

$$V_h = nA_s f_y(\sin\alpha + \mu\cos\alpha) \tag{3}$$

in which $\mu = \tan(b + \gamma_f)$ and b is the inclination angle of the top sliding interface of module III. Equation (3) can be further written into:

$$V_h = A\sin(\alpha + \gamma) \tag{4}$$

where $\gamma = \beta + \gamma_f$ and $A = nA_s f_y\sqrt{1 + \mu^2}$. From Equation (4), it can be found that the load capacity increases with the inclination angle of the sliding interface and the number, cross-sectional area, and yield strength of the dowel bars. Prior to yielding of the dowel bars, the stiffness of the superstructure, and thus the fundamental frequency of a bridge system, increases with the increase of the dowel bar prestress level in the shear key. The preferred minimum and maximum load applied on the shear key under tsunami loading are $A\sin\gamma$ and A, respectively. These loads correspond to two design states of the shear key: dowel bar yielding and ultimate load capacity. The hydrodynamic forces on a costal bridge deck in the horizontal and vertical directions due to tsunami inundation, represented by a solitary wave, can be obtained from Xiang et al. (2020). The allocation of hydrodynamic forces to each

shear key is carefully chosen within a range of the minimum and maximum loads applied on the shear key. This selection ensures efficient energy dissipation when the dowel bars yield, and prevents any sudden failures, such as concrete rupture and dowel bar breakage.

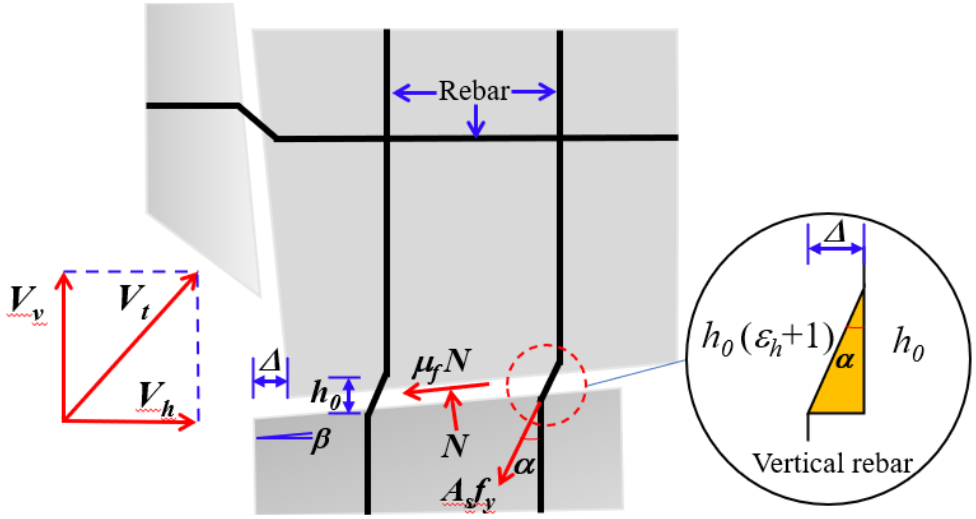

Figure 2.2 The working principle of the shear key

2.1.3 Bridge deck

The experimental sample of the bridge superstructure was originally designed by Bradner et al. (2011) based on the prototype dimensions of the Escambia Bay I-10 bridge provided by the Florida Department of Transportation. The geometry of the bridge superstructure used in this experiment was 1/5 of the prototype dimensions, as shown in Table 2.1, and the weight of the superstructure was approximately two tons.

Table 2.1 Dimensions of the bridge superstructure

Parameter	SI (m)
Width	1.94
Span length	3.45
Deck thickness	0.05
Girder height	0.23
Girder spacing	0.37
Safety barrier height	0.05
Total height at front edge	0.33

2.1.4 Material Tests

High-strength concrete will be used to cast SMART shear keys to prevent the shear failure or other premature failures before the steel dowel bars yield. In this study, high-strength concrete mixed with stainless steel fibers (13 mm in diameter and 0.2 mm in length) was adopted. Table 2.2 lists the material properties of the high-strength concrete. The splitting and compressive strength of fiber-reinforced concrete were 7.4 MPa and 62.3 MPa with a standard deviation of 0.3 MPa and 2.7 MPa, respectively. The yield strength and ultimate tensile strength of the steel dowel bars were 450.0 MPa and 965.8 MPa with a standard deviation of 3.3 MPa and 32.6 MPa, respectively. Figure 2.3(a, b, c) shows the experimental setups of the concrete splitting, comprehensive, and steel tension tests.

Table 2.2 Material properties for the SMART shear key

Material properties	Mean (MPa)	Standard deviation (MPa)
f_t	7.4	0.3
f'_c	62.3	2.7
f_y	450.0	3.3
f_u	965.8	32.6

Note: f_t and f'_c are the splitting and compressive strengths of steel fiber reinforced concrete, and f_y and f_u are the yield and ultimate strengths of steel bars.

(a) (b) (c)

Figure 2.3 Experimental setups for (a) concrete splitting test, (b) concrete compressive test, and (c) steel bar tension test

2.1.5 Design and Fabrication of SMART shear keys

Tsunami loading on a girder bridge is related to the wave height, bridge deck dimension, and deck vertical clearance above water level as mentioned by Xiang et al. (2020). Based on the information of the bridge and tsunami loads, the vertical and horizontal loads applied on the bridge deck can be calculated from the empirical equation in Xiang et al. (2020). With a preferred load range proposed in this study, the number, mechanical property, and size of dowel bars in each shear key can then be determined (Chen and Yuan 2018). The size of each module can be standardized in future applications. The design considerations of

each module include: 1) optimized energy dissipation through a selection of both an inclination angle and a dowel bar prestress level as well as displacement and force constraints under multiple hazards, 2) the concrete cover of dowel bars is thick enough to prevent a brittle failure in concrete fracture, 3) the SMART shear key can be deployed closely to the bottom flange of bridge girders for engagement under lateral and vertical loads, and 4) each shear key module is light enough to be erected by one or two engineers for retrofitted projects.

Since the bridge superstructure used for simulated tsunami tests is in approximately 1/5 scale, the SMART shear key was scaled down proportionally in size as shown in Figure 2.4. As detailed in Figure 2.4(a), the 1/5-scale shear key is 148.7 mm (reduced from 700 mm) long in the horizontal loading direction. To control installation errors on the bridge model and ensure quality of the shear keys, modules I and III were made of steel plates instead of fiber-reinforced concrete. Module III was fixed and module II on top of module III was laterally pulled to slide at a nearly constant speed. Based on the friction force measured from an electric scale, the coefficient of friction between the fiber-reinforced concrete and steel was mf = 0.367, which is slightly lower than 0.4 between two dry fiber-reinforced concrete components. To mimic the wet working environment of shear keys under tsunami loading, water was splashed to the interface of modules II and III. Under the wet condition, mf is reduced to 0.275. The shear key was designed with two sliding interfaces with an inclination angle of b = 5° (Yuan and Chen 2018). Then, m and gas mentioned in Section 2.1 can be determined to be 0.371 and 20.4°, respectively. The size of the dowel bars was chosen based

on the scale effect from a full-size shear key design (Yuan et al. 2019). Two vertical steel bars of 6.35 mm (reduced from 32 mm) in diameter with a spacing of 57.8 mm passed through pre-set holes of 7.94 mm in diameter in modules II and III. Each steel bar was inserted into a soft/flexible plastic tube used to fill the gap between the steel bar and its surrounding concrete, thus minimizing direct impact. Two dowel bars were adopted in the vertical or horizontal direction to ensure: i) the cover thickness is large enough to avoid fiber-reinforced concrete fracture and ii) each module is stable through the dowel-bar plan. The preferred load range can be calculated based on Equation (4), which is between 10.2 and 29.3 kN. The vertical and horizontal peak hydrodynamic forces on the offshore side, accounting for the overturning moment effect, were estimated from the experimentally-validated equation (Xiang et al. 2020) to be 22 and 18 kN, respectively, when the maximum wave height was 0.72 m. Thus, one shear key on the offshore side and another on the onshore side would be sufficient. Considering a potential rotation of the bridge deck due to non-uniform wave impact, two SMART shear keys were employed on each side of the bridge deck. The assembled SMART shear key is presented in Figure 2.4(b).

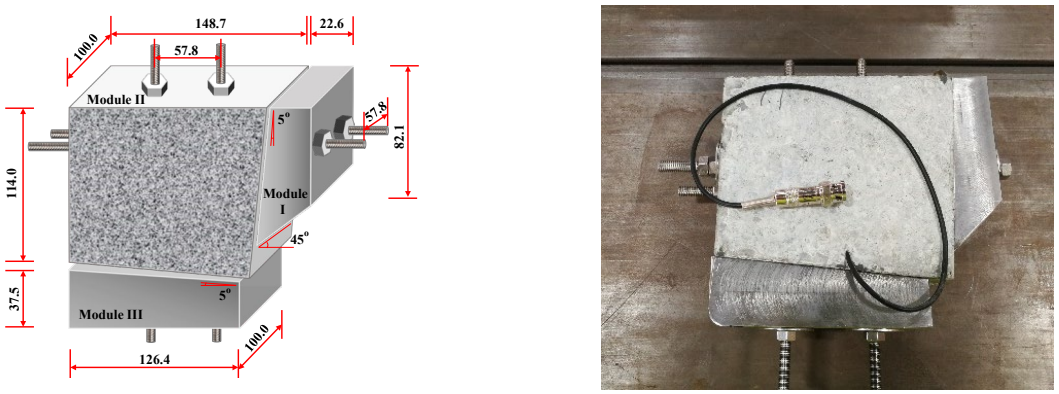

(a) (b)

Figure 2.4 A 1/5-scale SMART shear key: (a) schematic view and dimension (unit: mm) and (b) prototype assembly

2.2 Friction coefficient test for the interface between two modules

The coefficients of friction between the components of the SMART shear keys were measured with an electric scale. The measured coefficients of friction between the fiber-concrete component module II and the steel component module III was $\mu f = 0.367$, and the coefficients of friction between the two fiber-concretes was $\mu f = 0.4$. To better simulate the wet environment of the SMART shear keys under tsunami loads, water was dispersed and moistened between the contacting surfaces of each module, and the measured friction coefficient μf was reduced by 0.275. The shear keys are designed as two sliding interfaces with an inclination angle of $\beta = 5°$ (Yuan and Chen 2018). Then the values of μ and γ can be determined to be 0.371 and 20.4°, respectively.

2.3 Basic information for the large wave flume facility

A wave flume experimental facility at Oregon State University's Wave Research Laboratory generates isolated tsunami-like waves that act on the superstructure of a bridge

model. The wave flume is a hydraulic channel 104 m in length, 3.66 m in width, and 4.57 m in depth. The channel has 22 stations, each separated by 3.7 meters. Adjustable plates were also installed to create a workable bottom slope ranging from 0 to 1:12 at 1:36 intervals. The wave flume experimental facility is shown in Figure 2.5.

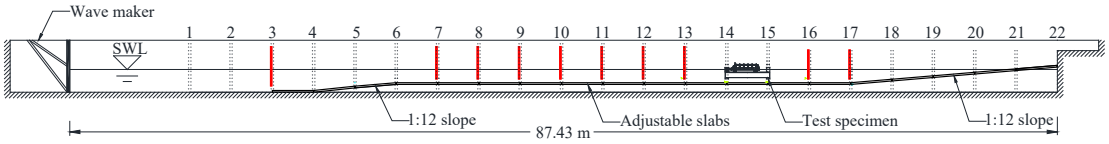

Figure 2.5 Schematic elevation view of the large wave flume

2.4 Instrumental setups

The test specimen of the bridge superstructure was originally designed by Bradner et al. (2011) based on the prototype dimensions of the I-10 Bridge over the Escambia Bay provided by the Florida Department of Transportation. The 1/5-scale was determined by the size of the large wave flume at Oregon State University. Six scaled AASHTO Type III girders were constructed and connected with two steel dowel bars that penetrate each of four evenly spaced diaphragms in one span. A removable L-shaped plate was designed to represent a safety barrier. Table 2.1 lists the dimensions of the test specimen. The weight of the superstructure is approximately 2 metric tons. Figure 2.6 shows the schematic elevation view of the experimental and instrumentational setup. The six girders rested on a pair of bent cap beams that are two HSS7×5×1/2 steel members. Four SMART shear keys were arranged approximately 300 mm away from the corners of external I-shaped girders in the

y-axial direction. Module III of each shear key was vertically fixed on four L-shaped steel plates that were firmly bolted on the bent caps. Module I of the shear key that perfectly fits into the shape of the girder bottom flange will limit both horizontal and vertical displacements of the test specimen subjected to tsunami loadings. Six load cells (LCs) were deployed not only to measure overall forces on the specimen, but also to prevent the bent caps from sliding off. Two LCs with a load capacity of 44 kN were used to measure horizontal forces acting on the bent caps at mid-height. The LCs were mounted between the bent caps and end anchorage blocks that were bolted to each side of the large wave flume wall. Four remaining LCs with a load capacity of 89 kN were employed to monitor vertical forces from offshore and onshore girders, which were installed between the bent caps and guide rails that attached to two W18×76 steel reaction frames bolted to the side walls. The LC readings were positive when tensioned and negative when compressed. All the LCs were set to zero at the beginning of each flume test at a specific wave height.

Ten wave gauges (WGs) based on twin-wire resistances were installed along the right-side wall (when looking downstream) at station marks 3, 7, 8, 9, 10, 11, 12, 13, 16, and 17 (see Figure 2.5). As shown in Figure 2.6, a total of three Acoustic Doppler Velocimeters (ADVs) were used to capture the velocities of fluid particles in three spatial directions around the bridge superstructure. All the ADVs were installed at 1.20 m deep. Longitudinally, ADV 2 was placed approximately 0.10 m onshore of the front edge of the bridge. ADV1 and ADV2 were spaced at 4.92 m and ADV2 and ADV3 were spaced at 6.18 m. Two three-axial accelerometers (ACCs) were installed on the top of the bridge deck 0.55 m apart from the

centerline of the superstructure to obtain the acceleration response of the bridge deck. Four string pots were installed to measure both the offshore and onshore displacements of the bridge superstructure both horizontally and vertically. Each string pot was fixed at the same object like the horizontal load cells. Thus, the displacement measurement represents a combination of the shear key sliding and the load cell deformation. With negligible load cell deformation, the string pot readings represent the sliding displacements in SMART shear keys. The data acquisition system (NI PXI-6259 module, National Instrument) was used to collect data at a sampling rate of 1,000 Hz. Figure 2.7(a, b, c, d, e) depicts the installed instrumentation.

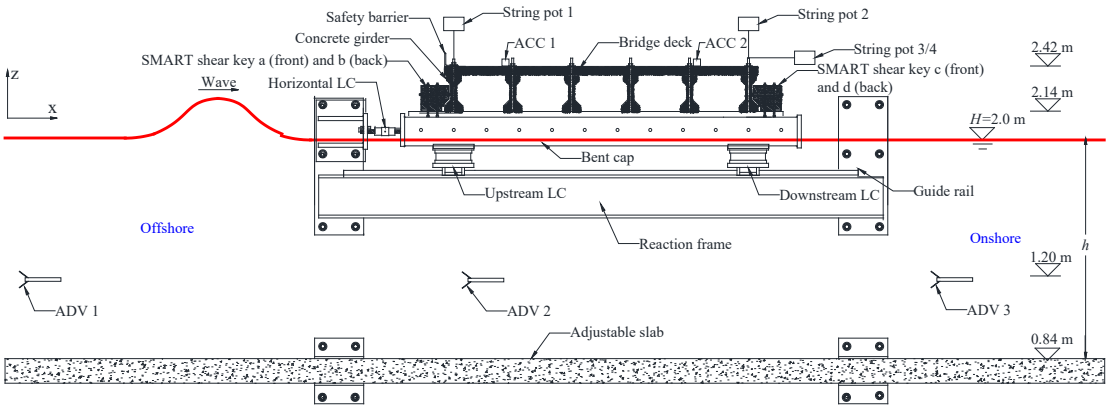

Figure 2.6 Schematic elevation view of experimental and instrumentational setups

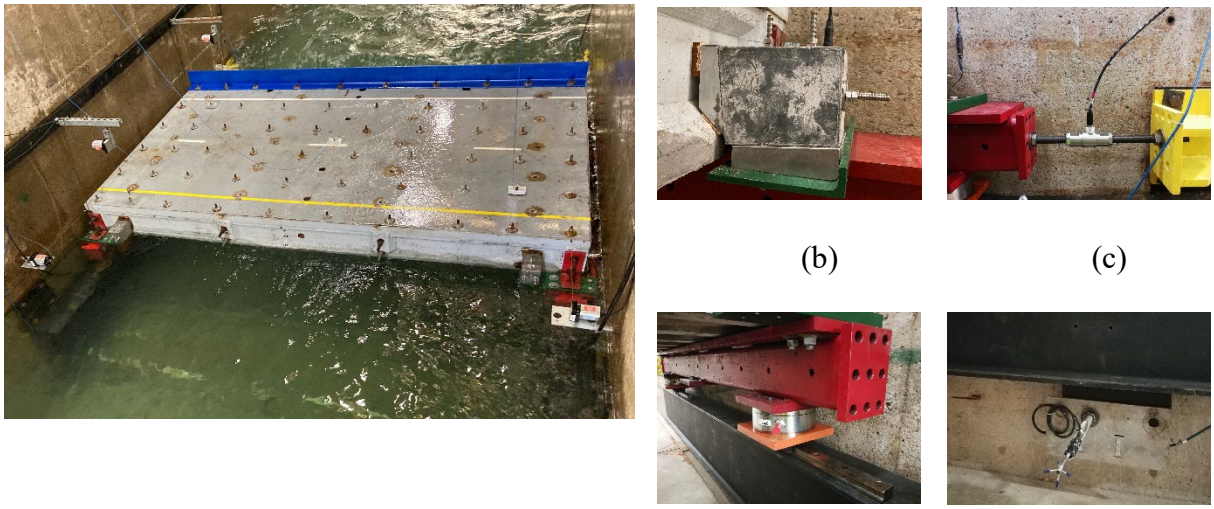

(a) (b) (c) (d) (e)

Figure 2.7 Installed instrumentation: (a) overview, (b) SMART shear key, (c) horizontal load cell, (d) vertical load cell, and (e) ADV

Chapter 3 Performance of SMART Shear Keys in Concrete Bridge under Tsunami Loading

3.1 Experimental program

3.1.1 Wave height and wave form

This test was conducted at the Wave Research Laboratory at Oregon State University, with the static water level (SWL) set at H = 2.0 m. Tsunami-like isolated waves with a magnitude level of four and wave heights of 0.27 m, 0.42 m, 0.57 m, and 0.72 m were applied to the reinforced concrete bridge. A wave height of 0.27 m indicates that it is parallel to the contact surface of Module II and Module III of the shear Ken, and a wave height of 0.42 m indicates that the wave height is flush with the bridge deck slab. Repeated tests at a constant nominal wave height revealed the actual wave heights and wave forms induced by the wave generator were essentially the same (Istrati et al. 2018). Therefore, only representative wave heights corresponding to SMART shear keys prestressed at 200 MPa are presented to save space. Figure 3.1 shows the wave heights over time in four cases, which were measured by wave gauges at Station Marks 3, 7-13, and 16-17. As expected, the wave height increased with the increase of nominal wave height, h. For each case, the first peak of the wave form was lower than h by less than 1%. The water height of the following waves between Station Mark 7 and 13 rose. This wave shoaling resulted from the 1:12 slope between Station Mark 4 and 6. The wave height at Station Marks 16 and 17 subsided after the wave pounded on the bridge model due to energy loss.

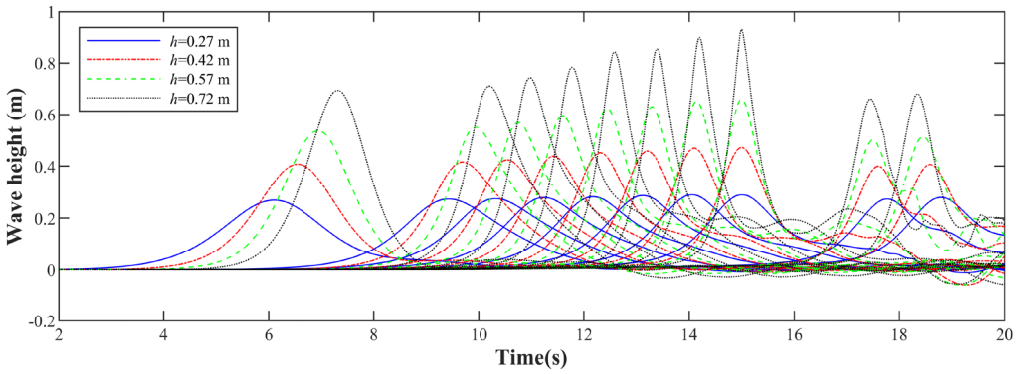

Figure 3.1 Typical wave forms measured from wave gauges at different nominal wave heights

3.1.2 Acoustic Doppler Velocimeters

Figure 3.2 presents the longitudinal (x-directional) velocities measured from ADV 1-3, corresponding to different prestress levels in SMART shear keys and different nominal wave heights. The outputs of the ADV1 and ADV3 were essentially independent of the prestress level applied on the SMART shear key. This indicated the consistency and repeatability of the loading input and wave propagation between various test cases at different prestress levels. Generally, the peak velocity from the ADVs increased with the increase of h. Due to energy dissipation, the velocity of the fluid decreased as the wave propagated from offshore to onshore. ADV2 readings appear affected locally by the prestress level, particularly at high water levels. Specifically, the velocity output from the ADV2 fluctuated at approximately 18 s when h≥0.42 m. This was likely attributable to the slip behavior of the SMART shear key. When h=0.27 m, the wave height was too low to cause a significant slip in the SMART shear key.

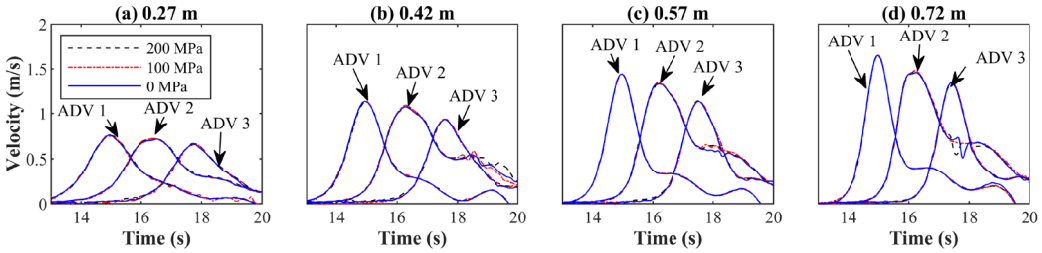

Figure 3.2 ADV outputs at various wave heights and prestress levels on the SMART shear key

3.2 Results and discussions for structural response

3.2.1 Structural responses

The acceleration, load, displacement, load-displacement hysteresis responses, and relationship between these responses of the bridge model were analyzed to demonstrate the role of the SMART shear key to potentially mitigate tsunami hazards.

3.2.2 Acceleration response

The experimental results show that by analyzing the measured accelerations of the bridge under wet conditions by Fast Fourier Transform, the intrinsic frequencies of the bridge under 0, 100, and 200 MPa prestressed can be determined for the SMART shear keys. The resulting natural frequencies are presented in Table 3.1. The measured intrinsic frequencies show a decrease in intrinsic frequency with decreasing levels of prestress on the SMART shear keys, which was mainly due to increased energy dissipation from reduced stiffness and increased friction. these fundamental frequencies in horizontal and vertical mode were 135 and 25 Hz, respectively (Bradneret al. 2011). Horizontal accelerations on the offshore side are presented in Figure 3.3. When h = 0.27 m, the acceleration response is small and

essentially the same regardless of the level of prestress applied to the shear keys. When h ≥ 0.42 m, there was a significant difference in the strength of the water wave at different prestress levels after the water wave reached the bridge bank. Specifically, the peak acceleration at 0 MPa prestress level was significantly higher than that at 200 MPa and 100 MPa prestress levels. In addition, the phase difference at different prestress levels was about 16.2 s.

Table 3.1 The first three natural frequencies at different prestress levels

Mode	Frequency (Hz)		
	200 MPa	100 MPa	0 MPa
Horizontal movement	134.9	134.2	132.8
Vertical movement	20.8	20.6	17.6
Rotation about the bridge centerline	34.3	33.7	32.7

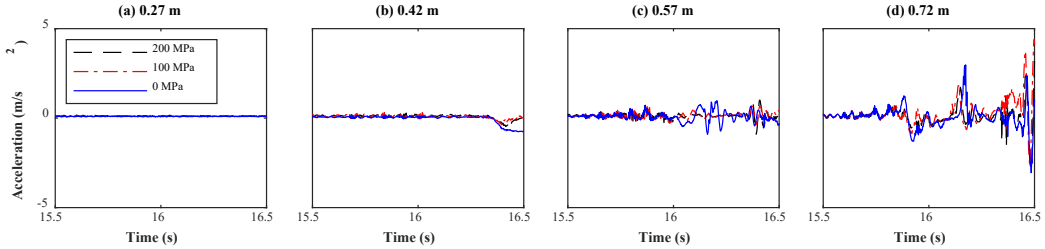

Figure 3.3 Horizontal accelerations on the offshore side

The vertical acceleration response on offshore and onshore (shown in Figure 3.4 and Figure 3.5) yielded similar results, with the vertical acceleration on the offshore side being twice that on the onshore side.

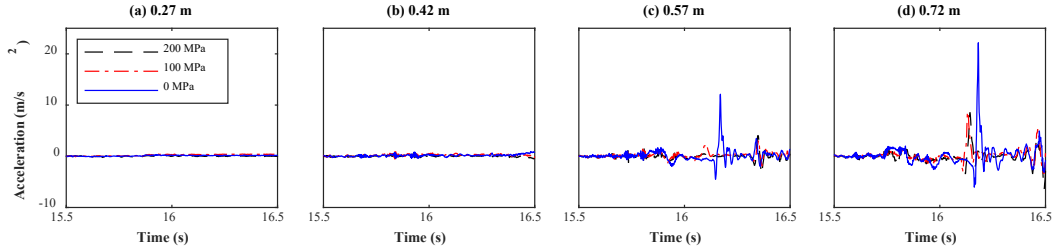

Figure 3.4 Vertical accelerations on the offshore side

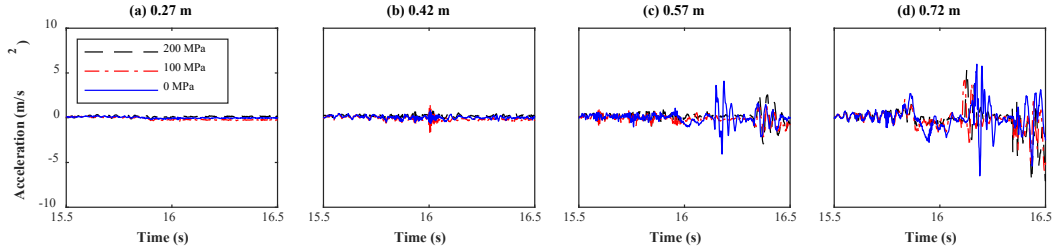

Figure 3.5 Vertical accelerations on the onshore side

To further decipher the frequency content and underlying physics, the normalized frequency spectra of horizontal and vertical acceleration responses between 15.5 s and 16.5 s are presented in Figure 3.6(a, b) when h=0.72 m. As expected, the frequency response was generally higher around the natural frequencies for vertical vibration as listed in Table 2.2. The dominant low-frequency component at approximately 1 Hz was generated by a quasi-static component of the solitary wave. The frequency spectrum at no prestress was more concentrated at a lower range of 5 Hz to 35 Hz, compared with the other two prestress levels. This results in a different load response, which will be demonstrated in the following section.

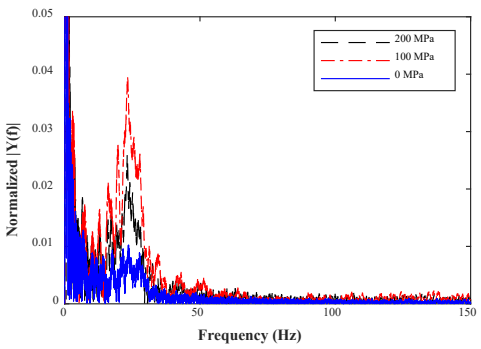

(a)

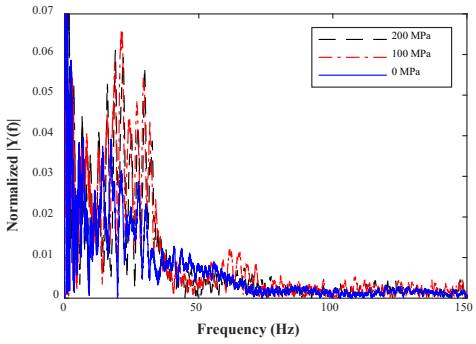

(b)

Figure 3.6 Fourier spectra of: (a) horizontal acceleration and (b) vertical acceleration

3.2.3 Load response

The horizontal load output between 15 and 17 seconds is shown in Figure 3.7, The load amplitude increases with increasing nominal wave height. This is because the hydrodynamic forces are too small to produce significant slip between the modules. Therefore, when h ≤ 0.42 m, the load response is independent of the prestress level applied to the SMART key; when h = 0.57 m and no prestress is applied to the SMART key, the load response starts to fluctuate up and down significantly around 16 s; when h = 0.72 m, the load fluctuation starts to fluctuate around 15.8 s due to the viscous-slip phase transition of shear keys caused by water splashing. Significant vibration occurs around 16.5 s when the wave just passes through the bridge model.

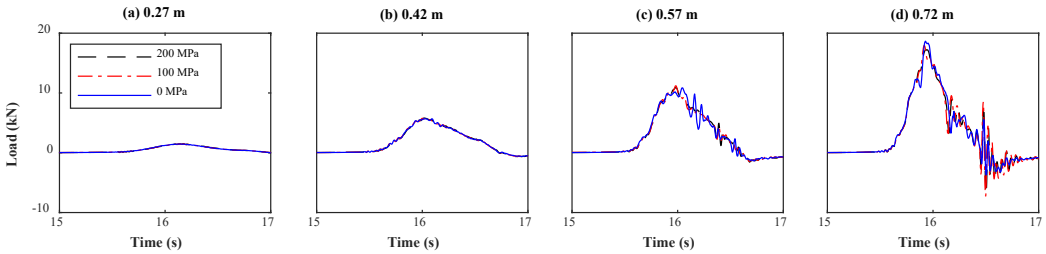

Figure 3.7 Horizontal load outputs between 15 to 17 s

The vertical load output on the offshore and onshore side between 15 and 17 s is presented in Figure 3.8 and Figure 3.9. When h = 0.27 m, the top of the bridge deck cannot be reached because the wave height is too low. When h ≥ 0.42 m, the short-term slamming force increases with increasing wave height. The load response was not affected by the prestress level until h ≥ 0.57 m. Similar responses can be seen in Figure 3.9 from the onshore load cells.

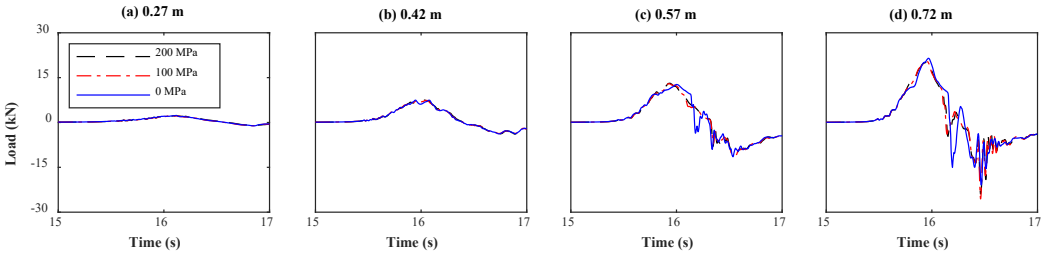

Figure 3.8 Vertical loads on the offshore side between 15 s and 17 s

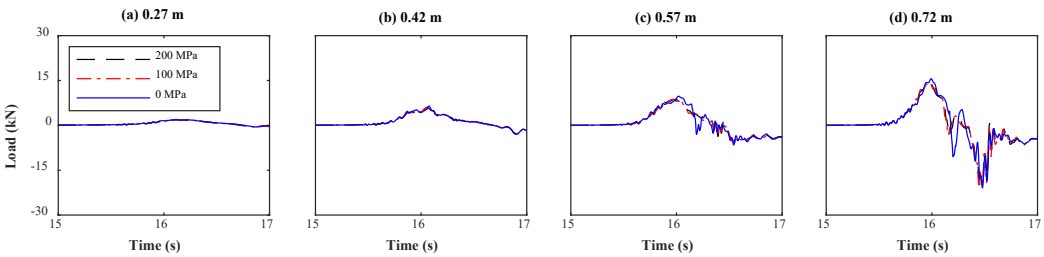

Figure 3.9 Vertical loads on the onshore side between 15 s and 17 s

Figure 3.10(a) and (b) demonstrate the maximum loads in the horizontal and vertical directions as a function of wave height at various prestress levels. The loads appear to increase linearly with the wave height, which agrees with the findings reported by Istrati et al. (2020). Notably, the prestress level does not significantly affect the load responses until a wave height of $h \geq 0.57$ m, as the hydrodynamic force is insufficient to induce a noticeable slip along the shear key interface. At a wave height level of 0.72 m, an increase in prestress level from 0 MPa to 200 MPa results in a decrease of 8.2% and 6.9% in horizontal and vertical loads, respectively. This decrease suggests that the shear key effectively reduces the tsunami load applied on the bridge once the slip-friction function of the shear key was activated.

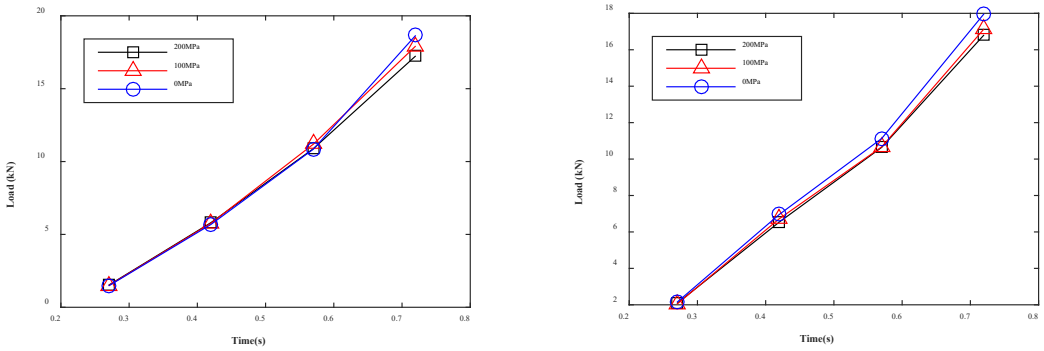

(a) (b)

Figure 3.10 Relationship between maximum wave force and wave height in (a) horizontal and (b) vertical direction

3.2.4 Displacement response

The horizontal displacement of the bridge deck along the flume is presented in Figure 3.11. When the wave height h = 0.27 m and h = 0.42 m, the horizontal displacement response is negligible. When the wave height h = 0.57 m, h = 0.72 m, the peak displacement response decreases as the prestress level increases from 0 MPa to 100 MPa; however, the peak displacement response remains essentially unchanged when the prestress level increases from 100 MPa to 200 MPa.

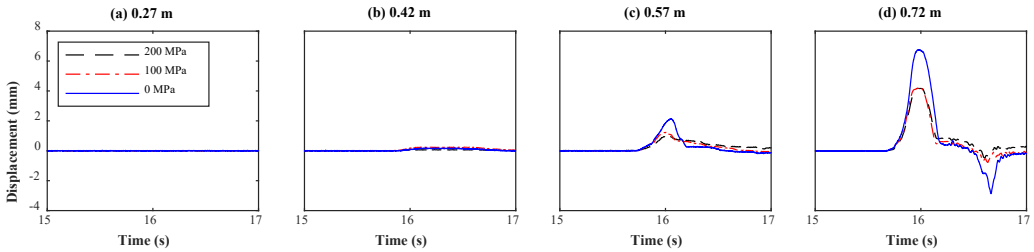

Figure 3.11 Horizontal displacements of the bridge deck along the flume

Figure 3.12 shows the vertical displacements of the bridge deck on the offshore side. The vertical displacement response is negligible when the wave height h = 0.27 m and h = 0.42 m. When the wave height h = 0.57 m and h = 0.72 m, the vertical response decreases with the increase of prestress level. A similar observation can be made from the onshore side vertical displacement of the bridge deck, as shown in Figure 3.13.

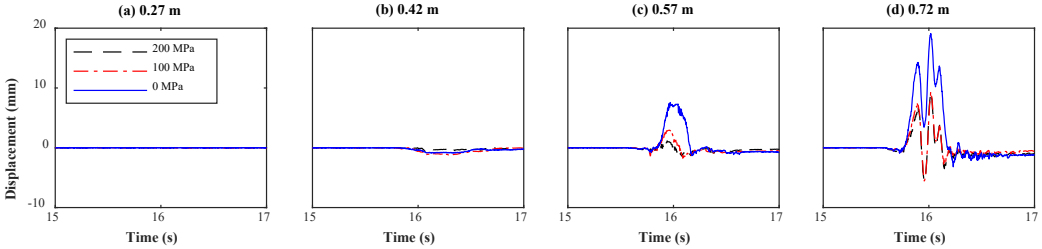

Figure 3.12 Vertical displacements on the offshore side

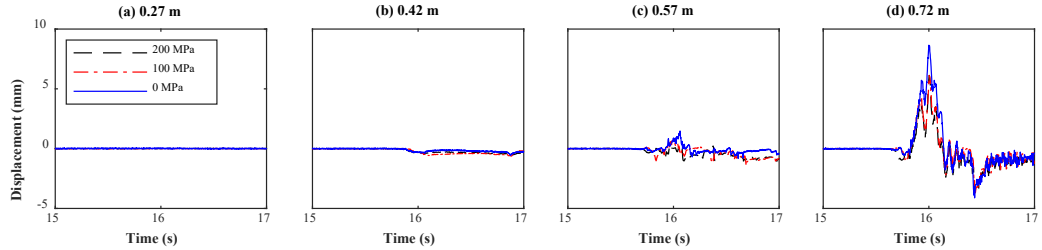

Figure 3.13 Vertical displacements on the onshore side

Figure 3.14(a) and (b) illustrate the maximum displacements as a function of wave height h at various prestress levels. Evidently, the horizontal or vertical displacement is nonlinearly related to the wave height. Furthermore, the addition of prestress on the shear key leads to a significant reduction in displacement of the bridge superstructure. At a wave height of h = 0.72 m, the bridge displacement is reduced by 60.9% and 88.7% in the horizontal and vertical directions, respectively.

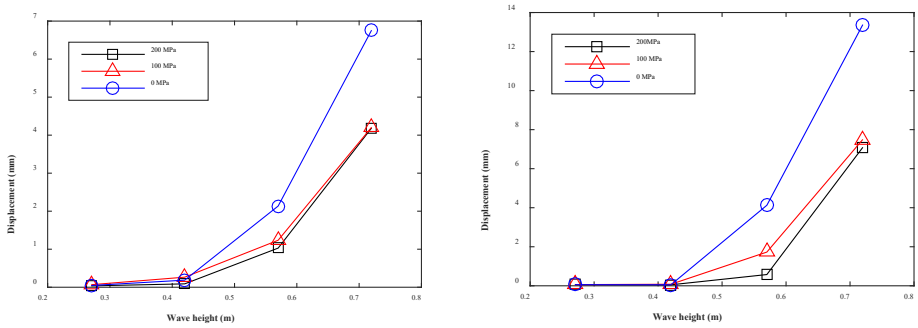

(a) Horizontal direction (b) Vertical direction

Figure 3.14 Relationship between maximum displacement and wave height in (a) horizontal and (b) vertical direction

3.2.5 Load-Displacement Hysteresis response

Under wave impacts, the load directly applied on the bridge deck will be transferred to the SMART shear keys. Therefore, the load-displacement response of the shear keys is the same as the bridge deck presented in Figure 3.15. In the horizontal direction, as seen in Figure 3.15(a), the responses of the shear keys when prestressed at 100 MPa and 200 MPa, respectively, agree as individually discussed in Section 4.2.2 and 4.2.3. At a prestress level of 0 MPa, the hysteresis shape is similar to that corresponding to a prestress level of 100 MPa and 200 MPa. However, the shear keys experienced a significantly larger hysteresis loop and thus more energy dissipation, while the maximum load is only slightly higher due to the control of friction force in the shear keys. In the vertical direction, the hysteresis loops under different prestress levels are compared in Figure 3.15(b). Although the contact area between Module II and III is larger than that between Module I and II, as seen in Figure 2.4, the coefficient of friction between concrete and steel materials is the same. Therefore, the friction

forces in the vertical and horizontal directions remain nearly the same under the same level of prestress in the shear keys. Figure 3.15 indicates that the SMART shear keys can dissipate a significant amount of input energy due to hydraulic loads while limiting the horizontal load transferred from the superstructure to its supporting substructure. When the shear keys are not prestressed, the bridge experiences 13.3 mm of uplifting, as indicated in Figure 3.15(b). This uplift is significantly reduced to 6-8 mm when the shear keys are prestressed from 100 to 200 MPa. The uplifting effect is the main reason why the hysteresis loops in the vertical direction differ in shape from those in the horizontal direction. According to the enclosed area of load-displacement curves presented in Figure 3.15, the energy dissipation of the SMART shear keys at three prestress levels ranging from 0 to 200 MPa can be calculated, which are 26.0 J, 16.7 J, and 17.2 J in the horizontal direction and 103.2 J, 39.5 J, and 37.9 J in the vertical direction. The potential energy of the bridge are 267.6 J, 144.5 J, and 141.9 J, based on the vertical displacement response of the bridge. The energy dissipated by the SMART shear keys is up to 32.5%, 28.0%, and 27.9% of the input energy that the bridge received from the tsunami loading.

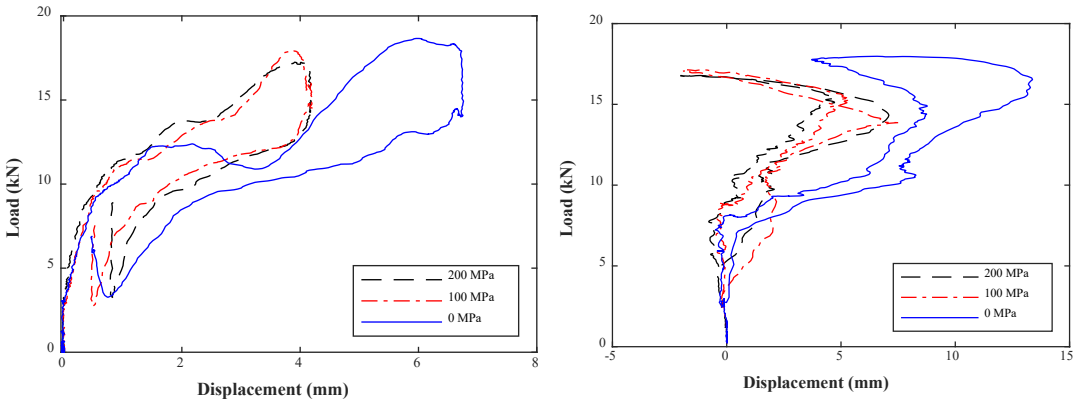

(a) Horizontal direction (b) Vertical direction

Figure 3.15 Load-displacement response for h=0.72 m at (a) horizontal; and (b) vertical direction

3.2.6 Relationships among Various Structural Responses

To fully understand the performance of a shear key under tsunami loadings, multiple structural responses (acceleration, load, displacement, and load-displacement hysteresis loops) in the X and Z directions are synchronized as shown in Figure 3.16 for a wave height of 0.72 m and a shear key prestress of 0 MPa. The X and Z responses at five critical instances represent the negligible initial response (point A/A′), the maximum tensile loading (point B/B′), the maximum positive displacement (point C/C′), the maximum compressive loading (point D/D′), and the maximum negative displacement (point E/E′). The acceleration responses as presented in Figure 3.16(a) are at the first significant valleys and the peaks when the bridge is subjected to the maximum tensile loading (i.e., point B/B′) and the maximum compressive loading (i.e., point D/D′), respectively, as shown in Figure 3.16(b). These observations indicate that the forces measured from the load cells are proportional to the inertial forces (opposite to the acceleration direction) at these moments. As shown in Figure

3.16(c), the peak horizontal displacement around 16 s arrived slightly behind the tensile loading (around 15.9 s, presented in Figure 3.16(b)) appears directly related to the inertial effect. However, in the vertical direction, the relative magnitude of gravity load and buoyancy changes the equilibrium condition, making the bridge deck float up and down in a few notable low-frequency cycles starting around 15.75 s. The largest peak acceleration at approximately 16.2 s between point B′ and D′ is caused by the impact of the uplifted bridge on the bent cap beam as the water subsides and the buoyancy force becomes lower than the bridge weight. This action is followed by a bounced-up motion before the bridge is set back on the bent cap beam around 16.4 s. After that, several high-frequency oscillations are observed as the wave passes around the structure. During this stage, the maximum compressive loading occurs (point D/D′) when the acceleration reaches to a peak value. As shown in Figure 3.16(c), the horizontal displacement becomes negative from point D to E as the wave leaves the bridge, creating a suction force. The residual displacement is zero in the horizontal direction and less than 1 mm in the vertical direction due to gravity effects. The uplifting effect causes the hysteresis response of the shear key to be significantly smaller in the horizontal direction than in the vertical direction, as shown in Figure 3.16(d, e).

On the offshore side, the vertical displacement of shear keys (a and b) dramatically increases from point B′ to C′ (see Figure 3.16(c)) when the vertical load slightly decreases (see Figure 3.16(b)). This indicates a significant slippage of the vertical shear interface between Module I and II, as evidenced by the notable permanent deformation on the plastic tubes covering the horizontal dowel bars, as shown in Figure 3.16(a, b). During that period,

the corresponding horizontal displacement slightly increases to its peak and then slightly decreases. On the onshore side, the vertical displacement of shear keys (c and d) is approximately 50% of that of shear keys (a and b) on the offshore side. Therefore, the bridge experiences a rocking motion about its centerline along the traffic direction. The combined rocking, horizontal and vertical displacements likely cause kinking of the vertical steel dowel bars on the shear keys (c and d), which are close to the bridge deck.

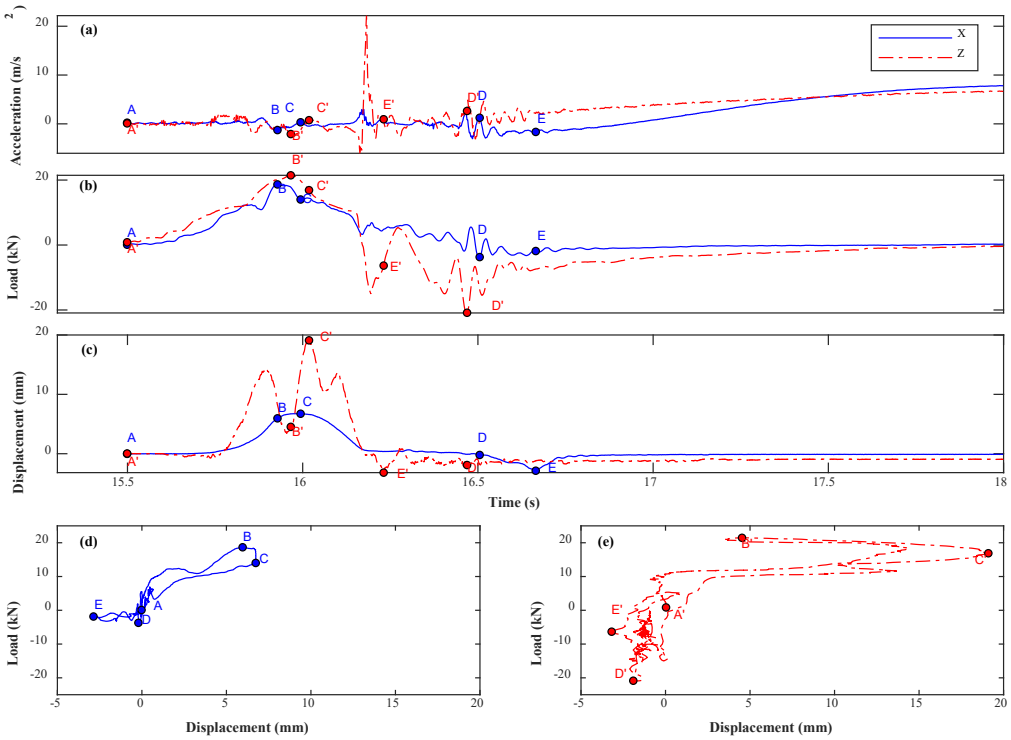

Figure 3.16 Structural response for h=0.72 m at 0 MPa prestress level of shear keys (a and b) on the offshore side: (a) acceleration; (b) load; (c) displacement (slip in shear key); (d) horizontal load-displacement hysteresis; (e) vertical load-displacement hysteresis

3.2.7 Failure mode of the SMART shear key

Figure 3.17 shows the failure modes of four shear keys. For the shear keys on the offshore side, as shown in Figure 3.17(a,b), the shear deformation of the plastic tubes on the outside of the horizontal dowel bars in the shear key is larger than that of the vertical dowel bars, which is attributed to the predominance of buoyancy forces in the vertical direction on the offshore side. For the shear key on the onshore side, the shear deformation of the plastic tubes outside the vertical bar in the shear key is larger than that of the horizontal bar as shown in Figure 3.17(c, d). As shown in Figure 3.17(c), a vertical bar closer to the bridge deck experienced significant buckling due to the significant increase in vertical and horizontal displacement. The external plastic tube of the anchor rod closer to the bridge deck even fractured, as seen in Figure 3.17(d). These observations indicate that the shear key dowels closer to the bridge deck on the onshore side were subjected to greater loads. Some concrete powder was generated by friction on the contact surfaces of Modules I and III. In addition, the brighter color of the concrete surface on Module II was also due to the effect of friction at the interface.

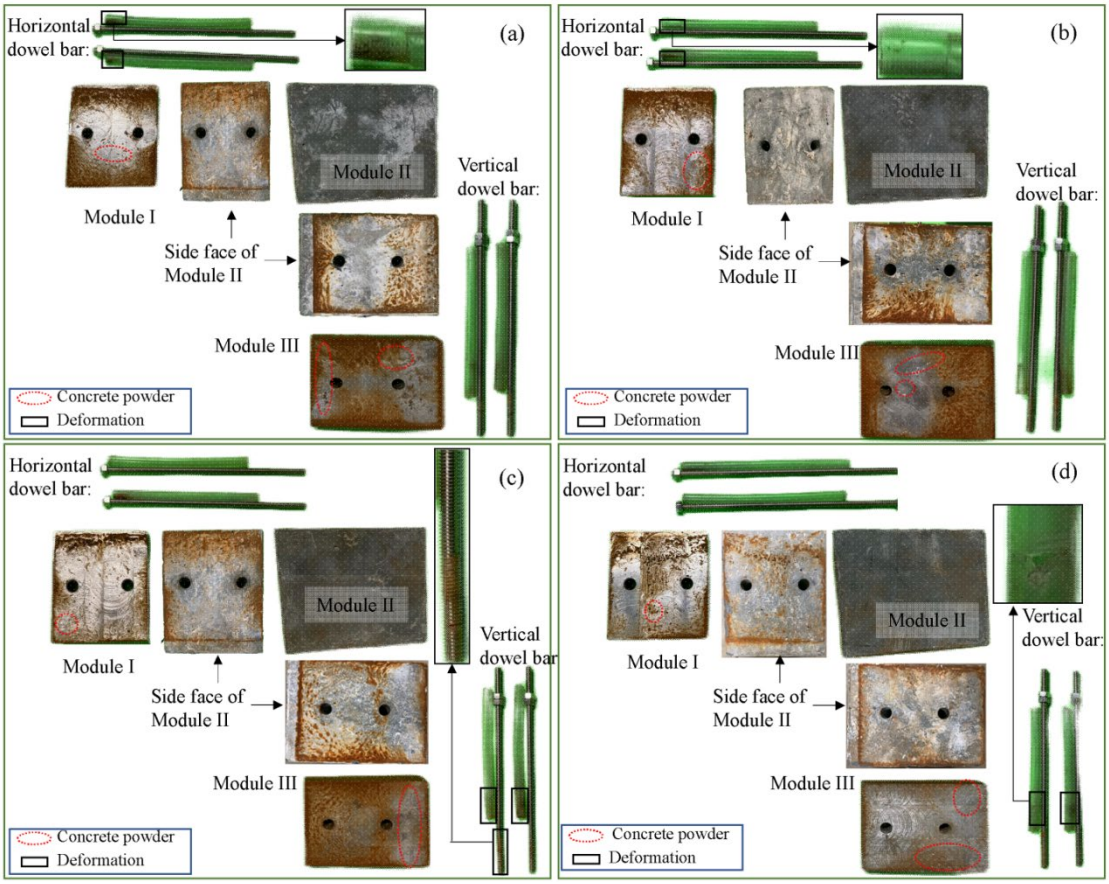

Figure 3.17 Failure modes of four SMART shear keys: (a) and (b) on the offshore side, and (c) and (d) on the onshore side

3.3 Summary

In this report, SMART shear keys are introduced to control the movement of girder bridges and the load transfer from the bridge substructure to substructure. The performance of the shear keys was experimentally evaluated through the 1/5-scale RC bridge model subjected to a series of tsunami-like solitary waves. Based on the experimental results and data analysis, the following conclusions can be drawn.

1. At a wave height of 0.72 m, the controllable friction mechanism of SMART shear keys by increasing a dowel bar prestress from 0 MPa to 200 MPa effectively reduced the load transferred from the superstructure to substructure of the bridge by 8.2% and 6.9% and reduced the bridge displacement by 60.9% and 88.7% in the horizontal and vertical directions, respectively. The residual displacement was zero in the horizontal direction and less than 1 mm in the vertical direction due to gravity effects.

2. The prestress levels in SMART shear keys changed the stiffness of the bridge system. As a result, the natural frequency of the bridge increased up to 18% when the shear keys were prestressed from 0 MPa to 200 MPa. The load-displacement hysteresis loop area (an indication of damping ratio) was reduced by 134%.

3. In comparison with the 'fixed' support of the bridge, the use of SMART shear keys reduced the hydrodynamic energy applied on the bridge by 32.5%. The most effective range of prestress (controllability) of the shear keys was from 0 MPa to 100 MPa. Utilizing a pair of SMART shear keys, the deck displacement, hydrodynamic load transferred from superstructure to substructure, and friction-dissipated energy of the 1/5-scale bridge model could be controlled under tsunami loads applied both horizontally and vertically.

Further studies are required to extend the obtained results from the 1/5-scale bridge model to its prototype due to scaling effects (Martinelli et al. 2010; Takahashi et al. 1985). For engineering applications, three critical factors must be investigated. First, current findings are limited to the effect of unbroken solitary waves only. More realistic tsunami-like bores considering the difference in wavelength (Madsen et al. 2008; Madsen and Schaffer 2010;

Chan and Liu 2012) and applied force (Leschka and Oumeraci 2014; Istrati and Buckle, 2019) must be studied. Second, a comprehensive design method and procedure must be formulated for a controllable tradeoff of deck displacement and substructure force under multiple hazards, such as earthquake and tsunami loads. Third, the bridge model including SMART shear keys was tested in a two-dimensional flume to understand its force transfer and overall displacement and did not account for three-dimensional phenomena, such as river channelization and bridge skew (Motley et al. 2016), so that could be a future focus of study.

References

Megally, S., Silva, P., & Seible, F. 2001. Seismic Response of Sacrificial Shear Keys in Bridge Abutments. UCSD/SSRP-2001/23, University of California, San Diego. Department of Structural Engineering.

Bozorgzadeh A, Megally S, Restrepo I J, et al. Capacity Evaluation of Exterior Sacrificial Shear Keys of Bridge Abutments[J]. Journal of Bridge Engineering,2006,11(5):555-565.

Silva, P. F., Megally, S., & Seible, F. 2009. Seismic performance of sacrificial exterior shear keys in bridge abutments. Earthquake Spectra, 25(3), 643–664. https://journals.sagepub.com/doi/abs/10.1193/1.3155405

Han, Q., Zhou, Y., Ou, Y., & Du, X. 2017. Seismic behavior of reinforced concrete sacrificial exterior shear keys of highway bridges. Engineering Structures, 139, 59–70. https://doi.org/https://doi.org/10.1016/j.engstruct.2017.02.034

Kottari, A., Shing, P. B., & Bromenschenkel, R. 2020. Shear Behavior of Exterior Non-Isolated Shear Keys in Bridge Abutments. *ACI Structural Journal*, *117*(2), 225–237. https://www.concrete.org/publications/internationalconcreteabstractsportal.aspx?m=details&id=51721317

Han, Q., Zhou, Y., Ou, Y., & Du, X. 2017. Seismic behavior of reinforced concrete sacrificial exterior shear keys of highway bridges. Engineering Structures, 139, 59–70. https://doi.org/https://doi.org/10.1016/j.engstruct.2017.02.034

Han, Q., Hu, M.-H., Wen, J.-N., & Du, X.-L. 2020. Seismic Capacity Evaluation of Interior Shear Keys for Highway Bridges. Journal of Earthquake Engineering, 24(6), 972–987. https://www.tandfonline.com/doi/abs/10.1080/13632469.2018.1453414

Han, Q., Hu, M.-H., Zhou, Y.-L., & Du, X.-L. 2018. Seismic Performance of Interior Shear Keys of Highway Bridges. ACI Structural Journal, 115(4), 1011–1021. https://www.concrete.org/publications/internationalconcreteabstractsportal/m/details/id/51701916

Caltrans. 2019. Seismic Design Criteria, Version 2.0, *California Department of Transportation, Sacramento*, CA

Kottari, A., M. Mavros, J. Murcia-Delso, and P. B. Shing. 2017. “Interface model for keys-slip and dowel-action behavior.” ACI Struct. J. 114 (4):1043–1053. https://doi.org/10.14359/51689870.

Xiang, T., D. Istrati, S. C. Yim, I. G. Buckle, and P. Lomonaco. 2020. “Tsunami loads on a

representative coastal bridge deck: Experimental study and validation of design equations." J. Waterway, Port, Coastal, Ocean Eng. 146 (5): 04020022. https://doi.org/10.1061/(ASCE)WW.1943-5460.0000560.

Bradner, C., T. Schumacher, D. Cox, and C. Higgins. 2011. "Experimental setup for a large-scale bridge superstructure model subjected to waves." J. Waterway, Port, Coastal, Ocean Eng. 137 (1): 3–11. https://doi.org/10.1061/(ASCE)WW.1943-5460.0000059.

Yuan, X., and G. Chen. 2018. "An adaptive SMART shear key and its mechanical properties for earthquake/Tsunami mitigation." In Proc.,7th World Conf. on Structural Control and Monitoring. Qingdao, China: Harbin Institute of Technology & Committee of Structural Control and Monitoring.

Yuan, X., Y. Zhu, G. Chen, H. Zhang, Z. Chen, and L. Fan. 2019. "SMART shear keys to prevent bridge girders from falling off during earthquakes and tsunami—Preliminary numerical simulations." In Proc., 3rd Int. Bridge Seismic Workshop. Zürich, Switzerland: International Association of Bridge Earthquake Engineering.

Xiang, T., D. Istrati, S. C. Yim, I. G. Buckle, and P. Lomonaco. 2020. "Tsunami loads on a representative coastal bridge deck: Experimental study and validation of design equations." J. Waterway, Port, Coastal, Ocean Eng. 146 (5): 04020022. https://doi.org/10.1061/(ASCE)WW.1943-5460.0000560.

Istrati, D., I. Buckle, P. Lomonaco, and S. Yim. 2018. "Deciphering the tsunami wave impact and associated connection forces in open-girder coastal bridges." J. Mar. Sci. Eng. 6 (4): 148. https://doi.org/10.3390/jmse6040148.

Martinelli, L., A. Lamberti, M. G. Gaeta, M. Tirindelli, J. Alderson, and S. Schimmels. 2011. "Wave loads on exposed jetties: Description of large scale experiments and preliminary results." Coastal Eng. Proc.32 (Jan): 18. https://doi.org/10.9753/icce.v32.structures.18.

Takahashi, S., K. Tanimoto, and S. Miyanaga. 1985. "Uplift wave forces due to compression of enclosed air layer and their similitude law." Coastal Eng. Jpn. 28 (1): 191–206. https://doi.org/10.1080/05785634.1985.11924415.

Madsen, A., D. R. Fuhrman, and H. A. Schäffer. 2008. "On the solitary wave paradigm for tsunamis." J. Geophys. Res.: Oceans 113: C12012. https://doi.org/10.1029/2008JC004932.

Madsen, A., and H. A. Schäffer. 2010. "Analytical solutions for tsunami run-up on a plane beach: Single waves, N-waves and transient waves."J. Fluid Mech. 645 (Feb): 27–57. https://doi.org/10.1017/S0022112009992485.

Chan, I. C., and L. F. Liu. 2012. “On the runup of long waves on a plane beach.” J. Geophys. Res.: Oceans 117 (C8): C08006. https://doi.org/10.1029/2012JC007994.

Leschka, S., and O. Hocine. 2014. “Solitary waves and bores passing three cylinders-effect of distance and arrangement.” In Proc., 34th Int. Conf. on Coastal Engineering. New York: Curran Associates.

Istrati, D., and I. Buckle. 2019. “Role of trapped air on the tsunami-induced transient loads and response of coastal bridges.” Geosciences 9 (4): 191. https://doi.org/10.3390/geosciences9040191.

Motley, M. R., H. K. Wong, X. Qin, A. O. Winter, and M. O. Eberhard.2016. “Tsunami-induced forces on skewed bridges.” J. Waterway, Port, Coastal, Ocean Eng. 142 (3): 04015025. https://doi.org/10.1061/(ASCE)WW.1943-5460.0000328.